High-resolution electron microscopy of energy-transducing proteins of *Escherichia coli*

By

Andrew L. Cottreau

Department of Microbiology and Immunology

Faculty of Medicine, McGill University, Montreal, QC

August 2011

A thesis submitted to McGill University in partial fulfillment of the requirements for the degree of Master of Science

Abstract

Transport of scarce nutrients such as iron and vitamin B_{12} across the outer membrane of Gram-negative bacteria depends on an integral cytoplasmic membrane protein complex: TonB-ExbB-ExbD. The proton motive force across the cytoplasmic membrane is transduced by this complex to TonB-dependent outer membrane receptors. High resolution structures of the C-terminal periplasmic domains of TonB and ExbD have been solved; structural information is lacking for the membrane-spanning regions of these two proteins and for ExbB. The stoichiometry of the complex, the native organization of TonB-ExbB-ExbD and the molecular mechanism of proton translocation remain undetermined. To investigate properties of ExbB-ExbD from *Escherichia coli*, we cloned *exbB* and *exbD* into different vectors and optimized expression of the recombinant proteins. By immobilized metal affinity chromatography in dodecyl maltoside, ExbB co-purified with His_6-tagged ExbD, thereby demonstrating their interactions *in vitro*. Size-exclusion chromatography identified a protein-detergent complex with a molecular weight of approximately 350 kDa. The molecular weight of His_6-tagged ExbB, also purified in dodecyl maltoside, was approximately 270 kDa. Negative-staining electron microscopy (EM) revealed uniform particles approximately 10 nm in diameter for the ExbB-ExbD complex. By low-dose single-particle analysis from high-resolution EM images, 2D averages and 3D reconstructions were generated for the ExbB-ExbD complex and for ExbB alone. A total of 45,321 particles for the ExbB-ExbD complex and 72,327 particles

for ExbB alone were collected by a computational single-particle selection system (SIGNATURE). Computational single particle analysis for resolution extension (SPARX) refined the 3D reconstructions. His_6-tagged ExbB showed particles approximately 9 nm in diameter and matched pentameric organization for the ExbB-ExbD complex. Preliminary analysis of the ExbB-ExbD complex by cryo-EM confirmed findings by negative-staining EM. Knowing the structural organization of the ExbB-ExbD complex will provide insights into the mechanism of energy-dependent nutrient import in bacteria.

Résumé

Le transport d'éléments nutritifs tels que le fer et la vitamine B_{12} au travers de la membrane externe (ME) des bactéries Gram-négatives tel *Escherichia coli*, dépend d'un complexe protéique intégral de la membrane cytoplasmique (MC): TonB-ExbB-ExbD. La force proton motrice qui traverse la MC est transmise par ce complexe aux récepteurs de la ME qui dépendent de TonB pour leur interaction. Les structures des domaines C-terminal périplasmique de TonB et ExbD ont été déterminées à haute résolution; mais, de l'information structurelle manque toujours sur les régions de ces deux protéines recouvertes par la MC et sur ExdB. La stœchiométrie du complexe, l'organisation indigène de TonB-ExbB-ExbD et le mécanisme moléculaire de la translocation des protons demeurent indéterminés. Pour étudier les propriétés du complexe d'ExbB-ExbD d'*E. coli*, nous avons cloné *exbB* et *exbD* dans différents vecteurs et optimisé leur expression. Par la chromatographie d'affinité de métal immobilisé, la co-purification de ExbB avec ExbD démontrait des interactions *in vitro*. La chromatographie d'exclusion stérique a identifié un complexe protéine-détergent d'une masse moléculaire approximative de 350 kDa pour ExbB-ExbD et de 270 kDa pour ExbB seul. L'utilisation d'un microscope électronique (MÉ) en coloration négative révèle des particules de taille uniformes d'approximativement 10 nm de diamètre pour le complexe d'ExbB-ExbD. Des reconstructions en 2D et 3D ont été générées pour le complexe d'ExbB-ExbD et d'ExbB seul. Ces reconstructions sont basées sur un total de 45,321 particules

pour le complexe d'ExbB-ExbD et de 72,327 pour ExbB assemblées par un système informatique pour la sélection de particules individuelles (SIGNATURE). ExbB démontrait des particules d'approximativement 9 nm de diamètre et, tout comme le complexe d'ExbB-ExbD, semble suggérer un arrangement pentamérique. L'analyse préliminaire du complexe d'ExbB-ExbD par cryo-MÉ confirme les observations par MÉ en coloration négative. En obtenant la structure du complexe d'ExbB-ExbD, nous pouvons amélioré notre compréhension des mécanismes moléculaires du transport des nutriments rares parmi les bactéries Gram-négatives.

Acknowledgements

I would like to thank my supervisor, Dr. James W. Coulton, for our insightful scientific discussions and for the support he has given me throughout my Master's research. I have greatly appreciated his dedication in embracing challenges at the leading edge of science.

Secondly, I wish to thank all members of Coulton laboratory, both past and present, for their support and for always maintaining a friendly scientific environment. They are, in alphabetical order: Damien Biot-Pelletier, Ernuo Cheng, Jacqueline Chung, Nathalie Croteau, Justin Deme, Jaesung Kim, Sofia Khalil, Wayne Mah, Maria Plesa, Isabelle Racine-Miousse, Aleksandr Sverzhinsky and Colins Vasquez. I wish to give further thanks to Damien Biot-Pelletier for mentoring me throughout the beginning of my Master's research. I also want to thank Aleksandr Sverzhinsky whom I have worked closely with in regards to our projects since his arrival in January, 2010. Furthermore, I wish to thank Jacqueline Chung for her valuable insight and extensive revision of my thesis.

I wish to give special thanks to our collaborator whom, along with Dr. Coulton, is a member of le groupe d'étude des protéines membranaires (GÉPROM), Dr. Isabelle Rouiller, Associate Professor, Department of Anatomy and Cell Biology, McGill University, assisted by Mihnea Bostina, staff scientist, Facility for Electron Microscopy Research (FEMR). Throughout my Master's research I have continued to interact directly with Drs. Rouiller and Bostina to

gain the hands-on experience required to operate two electron microscopes, and also to be able to computationally analyze the data I obtained. I must also thank all members of Dr. Rouiller's laboratory, who are, in alphabetical order: Kaustuv Basu, Brian Beckett, Lucien Fabre, and Driss Mountassif, for all their support and discussions on electron microscopy.

I wish to thank the National Center for Macromolecular Imaging for hosting a four day cryo-EM workshop I attended at the University of Houston, from March 13th-17th, 2011. I greatly benefitted from the opportunity to meet several software creators at the forefront of cryo-EM data analysis.

I also want give an enormous thank you to my parents, Karen and Terrence Cottreau, my sister Danielle, and my brother Thomas, for providing a healthy environment to learn and grow, and for always encouraging me in all of my endeavours.

Research in the Coulton Laboratory is supported by the Canadian Institute of Health Research (CIHR), and Canada Foundation for Innovation (CFI) provided infrastructure for the Facility for Electron Microscopy Research (FEMR). The DNA sequencing services at McGill University and Génome Québec Innovation Centre are acknowledged. Lastly, I thank GÉPROM, Fonds de la recherche en santé du Québec (FRSQ), and McGill University for all their financial support throughout my Master's research.

Table of Contents

Chapter 3 – Results

Chapter 4 – Discussion and summary

List of Tables and Figures

Page

Chapter 1: Literature review and introduction to conducted research

1.1 Cell envelope of Gram-negative bacteria

The bacterial cell envelope provides structural integrity essential for cell survival. Bacteria are classified into two groups, Gram-positive and Gram-negative, derived from differences in their structural organization and functional features in the cell envelope [1]. The cell envelope of Gram-positive bacteria is composed of a cytoplasmic membrane of lipid surrounded by a thick peptidoglycan layer. In comparison, the more complex cell envelope of Gram-negative bacteria, such as *Escherichia coli*, has two membranes; the outer membrane (OM) and cytoplasmic membrane (CM), are separated by the periplasm containing a thin peptidoglycan layer (Fig. 1).

The OM, in contact with the external environment, is the first line of defence to protect bacteria from physical and chemical stresses. The OM also serves to internally compartmentalize the cell [2]. Water and nutrients smaller than 600 Da passively diffuse across the OM, while larger compounds must be actively transported. To maintain cell stability, the OM is an asymmetrical bilayer containing phospholipids in the inner leaflet, and lipopolysaccharides (LPS) in the outer leaflet [3]. Also within the inner leaflet of the OM are lipoproteins responsible for forming bridges to the peptidoglycan layer. LPS is essential for many Gram-negative bacteria, with the exception of *Neisseria meningitidis*, and variations in structure are based on surrounding environmental conditions [4].

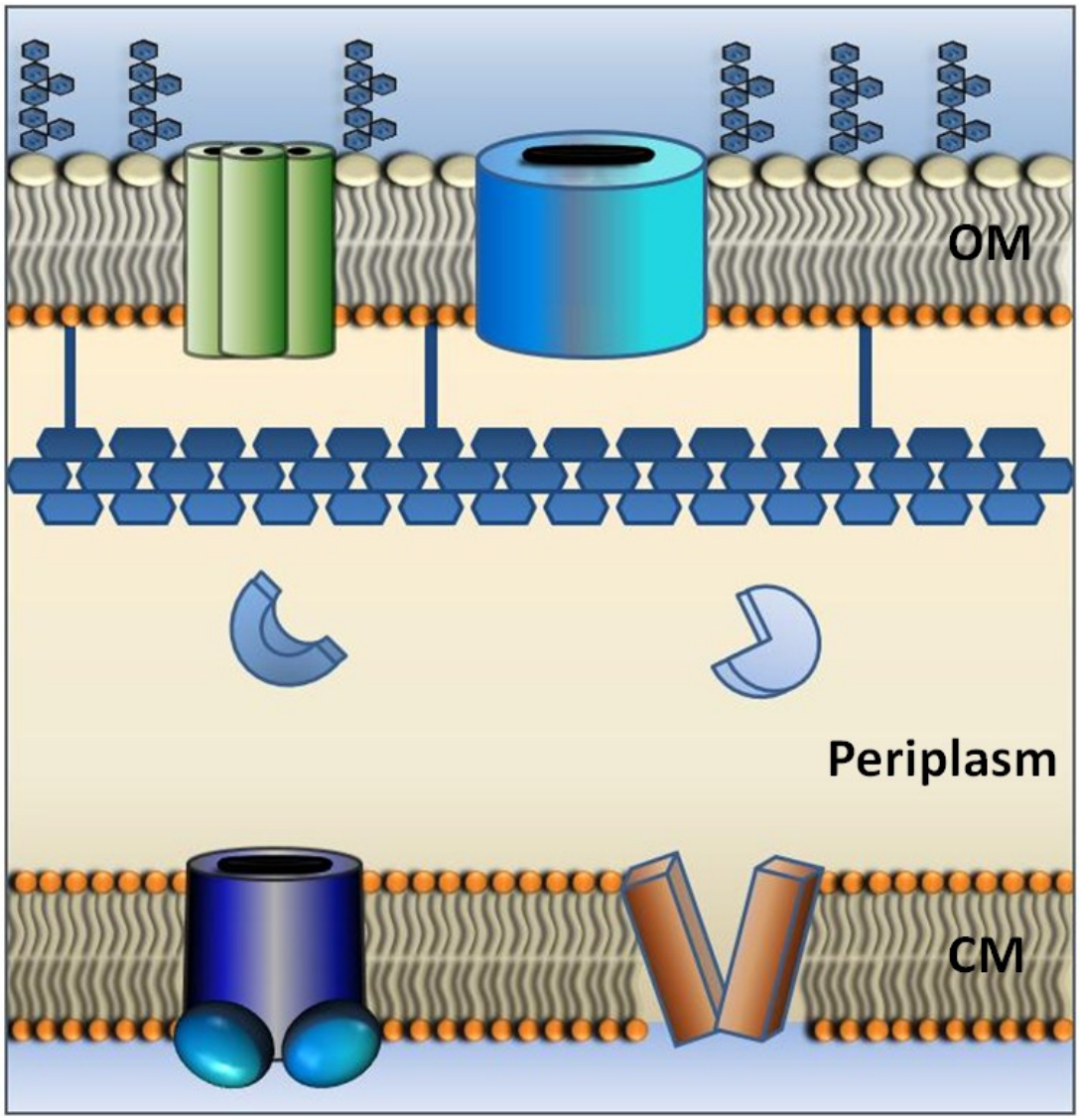

Figure 1: Gram-negative cell envelope. The outer membrane (OM) and cytoplasmic membrane (CM) are separated by the periplasm. The OM is an asymmetrical bilayer containing phospholipids (orange) and lipoprotein (blue bars) in the inner leaflet, and lipopolysaccharides (LPS; light brown) in the outer leaflet. A thin peptidoglycan layer (blue hexagons) is anchored to the OM via lipoprotein. OM proteins such as porins (green) and receptors (light blue) are necessary for passive and active transport respectively. Proteins in the periplasm are involved in nutrient transport (light purple). The CM is a phospholipid bilayer containing transmembrane proteins, and permeases (dark purple, brown) which are necessary for nutrient uptake into the inner cell.

LPS confers a negative charge to the OM and is separated into two distinct domains; lipid A is the hydrophobic domain embedded within the outer leaflet, and polysaccharide is the hydrophilic domain that extends out of the cell and into the extracellular environment. Lipid A has a lipid moiety structure and is responsible for the endotoxic effects of Gram-negative bacteria [3]. Transport of LPS is based on a group of family proteins: LptA, LptB, LptC, LptD, and LptE [5]. Deletion of any one of the Lpt proteins prevents LPS pathway assembly, causing a decrease in OM stability.

A key component of the Gram-negative cell envelope is the peptidoglycan layer contained in the periplasm. Its composition is a three-dimensional (3D) mesh of repeating disaccharides cross-linked by amino acid moieties [6]. This layer is essential for maintaining structural integrity of the cell envelope; given its resistance to tensile forces, the peptidoglycan layer counteracts the osmotic pressure located in the cytoplasm [7]. It is known that particles approximately 2 nm in diameter are able to passively diffuse through the peptidoglycan layer [8]. Also contained within the periplasm are numerous enzymes responsible for nutrient degradation and inhibiting toxic compounds adverse to the cell. In addition, the periplasm contains transport proteins that deliver nutrients, such as the periplasmic protein FhuD, for ferric iron transport, and BtuB, for vitamin B12 transport, to permeases embedded in the CM [9].

The CM is the final barrier of the cell envelope prior to entering the inner cell. This phospholipid bilayer is responsible for the transfer of compounds to

and from the cytoplasm. Many proteins in the CM are involved in the transport of nutrients, energy production, protein secretion, and lipid biosynthesis [10]. Transmembrane proteins spanning the CM harness energy from the electrochemical gradient, derived from the proton motive force (PMF), for ATP-synthesis and transport of essential nutrients. Proteins that are embedded in the CM, but do not span its entire length are known as membrane-associated proteins.

1.2 Nutrient import across the OM in Gram-negative bacteria

Import of nutrients from the external environment into the inner cell of Gram-negative bacteria can be achieved in two ways based on their MW: passive and active transport. Molecules less than 600 Da, which includes water, amino acids, lipids and carbohydrates, passively diffuse across the OM and enter the periplasm. Scarce nutrients including iron and vitamin B_{12} are essential for bacterial growth, but their complex mechanism of acquisition and required transport prevents passive diffusion across OM channels. As such, compounds greater than 600 Da must be actively transported across the OM, with energy derived from transmembrane ion potentials located in the CM.

1.21 Energy-independent transport

Water-filled transmembrane channels, known as porins, are β-barrel proteins located in the OM that allow for the passive diffusion of molecules smaller than 600 Da. All porins share the same overall β-barrel structure and are known to form homotrimers. Three porins that span the OM in *E. coli* have been well documented: OmpC, OmpF, and PhoE [11]. OmpC and OmpF demonstrate an affinity for cations, while PhoE has an affinity for anions. All three porins are homotrimeric, and each monomeric porin forms a β-barrel composed of 16 anti-parallel β-strands [12]. This anti-parallel β-strand configuration observed in porins allows for the open formation of a channel [13].

Unique to porins is the composition of the amino acids that interchange between polar and non-polar residues. This allows for non-polar residues to interact with the OM, while polar residues are situated within the porin channel. These polar residues can either prevent or allow entry of molecules specific to the given porin. Furthermore, there is a loop that extends into the inner channel that acts to influence both the size and composition of molecules passing through the porins.

Porins vary in specificity; some porins are non-specific and will allow the entry of any molecule that is less than 600 Da. Other porins are chemically selective and may only select one specific type of molecule, or a particular group of molecules. Specific channels allow for fast diffusion of a finite class of

molecules. One of these porins, ScrY, is a sucrose channel in strains of *E.coli* and *Salmonella* that use sucrose as a source of carbon [14]. ScrY has similar structure to the maltose channel, LamB, which is involved in the diffusion of maltose and maltodextrin into the cell [15]. Both ScrY and LamB are observed to be homotrimeric, with each monomer organized as a β-barrel consisting of 18 β-strands [16]. When comparing the inner channels of ScrY and LamB, both contain a structure known as a greasy-slide, which contains several aromatic residues extending into the lumen. Substrate selectivity between ScrY and LamB is structural dependant, as sucrose traversing the ScrY porin interacts with a pyranose ring located on the glucosyl residue that is not observed in LamB [16]. Furthermore, residues which prevent sucrose transport through LamB are not observed in ScrY. As such, it is the formation and removal of hydrogen bonds interacting with downstream residues of LamB that provides specificity to transport maltose and maltodextrin into the periplasm [17].

1.22 Iron transport: energy-dependent transport

The uptake of scarce nutrients larger than 600 Da, such as ferrichrome-iron and vitamin B_{12}, cannot be achieved via porins. There is also no source of energy available at the OM or within the periplasm given that there are no ATP-hydrolyzing proteins present or the potential formation of a proton gradient [18]. In *E. coli*, transporters are required to actively uptake these nutrients across the OM, a process that involves an OM receptor, a periplasmic binding protein and

an integral CM protein complex: TonB-ExbB-ExbD (Fig. 2). To facilitate the need for energy at the OM, ExbB and ExbD are proposed to harness the PMF to extend TonB across the periplasm; energy is then transduced from TonB to specific TonB-dependent receptors at the OM for nutrient uptake from the extracellular environment.

Iron is an essential nutrient for bacterial growth and survival, and is required in many processes including, metabolism, gene expression regulation and electron transport. There are two oxidative states of iron depending on conditions in the external environment: ferrous, Fe^{2+}, and ferric, Fe^{3+}. Ferrous iron is observed during anaerobic conditions, and is soluble for uptake into anaerobic bacteria. However, in aerobic conditions, ferric iron is produced, which is both insoluble and scarce with a concentration of 10^{-18} M in the external environment [19]. To alleviate this obstacle, bacteria produce siderophores that are soluble compounds of low molecular weight (MW). Bacteria produce three classes of siderophores: hydroxamate-type siderophores, such as ferricrocin involved in the iron uptake system of *E. coli*, catechol-type siderophores, such as aerobactin in *E. coli* involved in sequestering iron in areas such as the urinary tract, and dicarboxylic and tricarboxylic acids [20]. These compounds contain oxygen atoms that are able to effectively coordinate ferric iron ions. Transport of ferric iron across the OM requires the use of siderophores, which are released into the extracellular environment with a high binding affinity to ferric iron. These iron-siderophores are then actively transported across the OM through

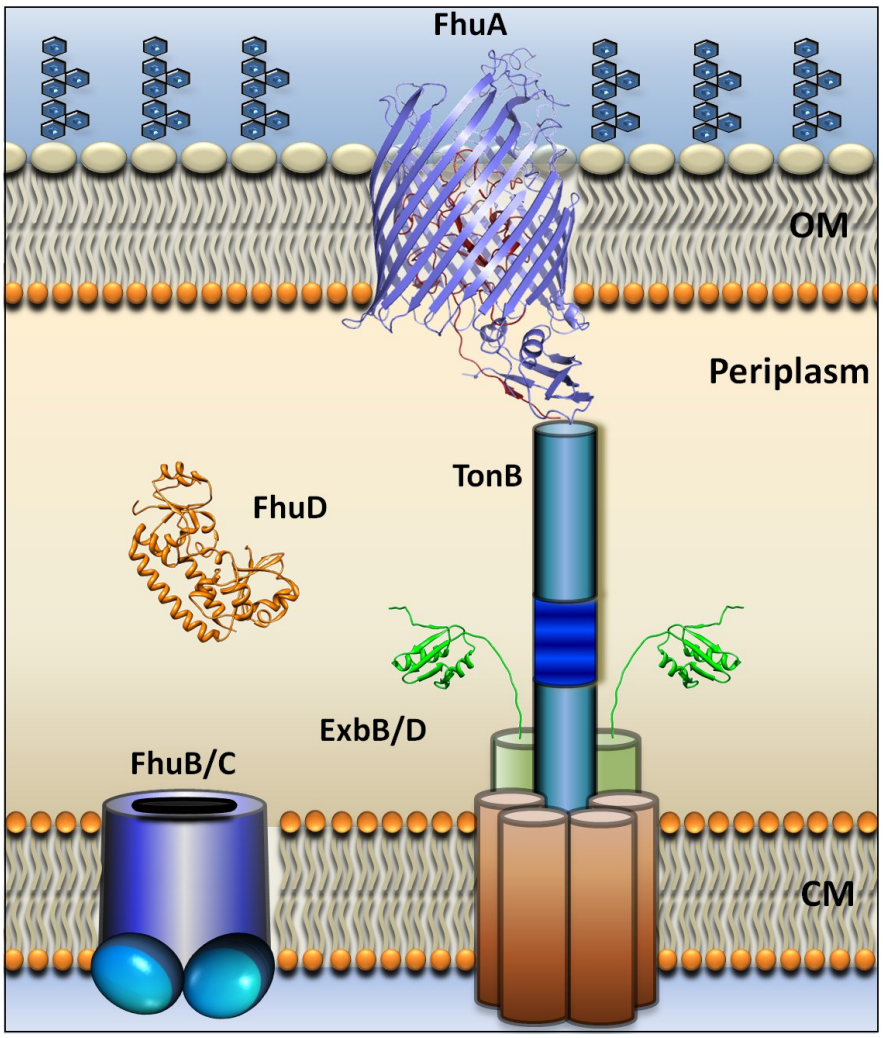

Figure 2. Iron uptake system in Gram-negative bacteria. Transporters involved in the active uptake of iron into the cell include an OM receptor, FhuA, a periplasmic binding protein, FhuD, an integral CM protein complex, TonB-ExbB-ExbD, and an ATP-binding cassette transporter complex FhuBC. Crystal structures display FhuA-TonB interactions (light purple; PDB code: 2GRX) involved in transporting iron-siderophore complexes into the periplasm, FhuD (orange; PDB code: 3G9Q) involved in transporting the iron-siderophore complex to FhuBC (dark purple), and the C-terminal end of two ExbD monomers (green; PDB code: 2PFU). ExbD in complex with ExbB (brown) is proposed to harness the proton motive to provide energy for the transport system. Unresolved structures are demonstrated as cylinders.

TonB-dependent receptors located at the OM. This process is necessary as the generation of a porin large enough to allow the passive diffusion of iron-siderophores across the OM would give entry to other large, non-specific molecules, including external toxicities that could compromise bacteria.

The ferrichrome OM receptor FhuA is one of three receptors, along with FecA and FepA, to transport siderophores across the OM in *E. coli*. These three OM receptors share high structural identity. The FhuA barrel is larger than any known porin with a height of 69 Å and an elliptical cross-section of 46 by 39 Å [21]. The shortest OM barrel is that of FecA, a ferric citrate receptor, with a height of 65 Å, and an elliptical cross-section of 35 by 47 Å [22]. Fep A, a ferric enterobactin receptor, is the tallest barrel with a height of 70 Å, and an elliptical cross-section of 30 by 40 Å.

Five receptors in *E. coli* strain K-12 bind with high affinity to various ligands whose interactions are involved with TonB; BtuB, vitamin B_{12} receptor, Cir, colicin I receptor, and previously described FhuA, FecA and FepA [23]. Five additional structures have been solved for TonB receptors of other bacterial species: FauA of *Bordetella pertussis*, involved in siderophore alcaligin secretion and binding, FptA and FpvA of *Pseudomonas aeruginosa*, involved in transport of ferric-siderophores pyochelin and pyoveridine respectively, and other proposed siderophore transport by HasR of *Serratia marcescens* and ShuA from *Shigella dysenteriae* [24]. As with all OM proteins, TonB-dependent receptors are

configured in a β-barrel formation. The channel is constructed from 22 anti-parallel β-strands, larger than 16 anti-parallel β-strand structures of several porins previously described. The N-terminal portions of these TonB-dependent receptors contain a globular domain that acts as a cork in the center of the channel, preventing the passive diffusion of large molecules [25]. When comparing crystal structures of OM receptors that are ligand-bound or unbound, OM receptors displayed distinct conformational changes suggesting that the open state occurs when the iron-siderophore is bound. Given that these are TonB-dependant OM receptors, the energy required for change in conformation to an open state is derived from the CM protein complex of ExbB and ExbD. These two proteins are proposed to harness the PMF to allow TonB to interact with the OM receptor. Interaction between TonB and the OM receptor is proposed to occur predominantly at amino acids five or six in the N-terminal end of the OM receptor at a site known as the TonB box [26].

While porins are typically observed in trimeric organization, FhuA has been determined to be monomeric. The crystal structure of FhuA bound with ferrichrome-iron was resolved to 2.7 Å (Fig.3), while the crystal structure of FhuA without substrate was resolved to 2.5 Å [21]. When ferrichrome-iron is bound to FhuA, interactions are readily observed at the binding pocket in loops extending into the extracellular environment. Furthermore, interactions at the cork domain act as binding sites for the uptake of ferrichrome-iron. With respect to the

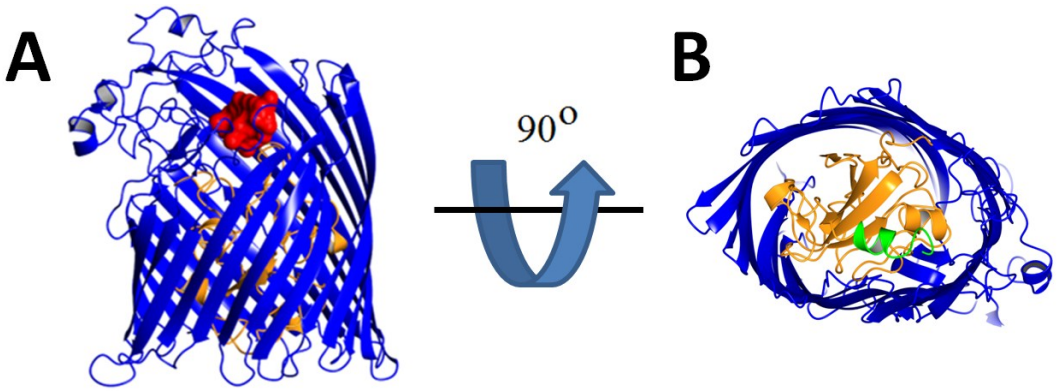

Figure 3. Crystal structure of TonB-dependent OM receptor FhuA. FhuA's monomeric organization viewed from the OM plane demonstrates 22 anti-parallel β-strands (blue) structure bound with ferrichrome (red) resolved to 2.7 Å (A). A 90° orientation demonstrates FhuA's lumen viewed from the periplasm (B). The cork domain is located in the center of the channel to prevent passive diffusion of large molecules (orange). N-terminal switch helix residues essential for FhuA-TonB interactions is also observed (green).

β-barrel structure of FhuA without ferrichrome-iron, very minor conformational changes are observed.

Binding of ferrichrome-iron causes an allosteric transition in the cork domain that provides entry for transport across the OM and into the periplasm. This mechanism is proposed to begin at the N-terminus of the cork domain, where binding of ferrichrome-iron causes the destabilization of the switch helix, a hydrophobic region consisting of residues 24 to 29 (Fig. 3B) [21]. Destabilization of the switch helix is achieved when interactions are disrupted between the binding pocket and the hydrophobic areas of the switch helix [27]. As a result, the switch helix unwinds 180° to allow interactions between the TonB box of FhuA with the C-terminal end of TonB.

A crystal structure demonstrating interaction of TonB-FhuA by way of the TonB box was recently resolved to 3.3 Å (Fig. 4) [28]. As previously stated, results were structurally similar to that of the OM receptors in *E. coli* FecA and FepA, but also to that of the vitamin B_{12} transport receptor, BtuB [29]. The ToB-FhuA structure showed significant conformational changes in the external loops exposed to the extracellular environment, and also the hydrophobic regions of the binding pocket of the cork domain. With the switch helix unwound, interaction between FhuA and TonB was shown through the TonB box. Interactions analyzed from the crystal structure suggest that a β-sheet is generated between the TonB box of FhuA and the C-terminal domain of TonB.

The resulting position of the C-terminal α-helix of TonB demonstrates that TonB interacts closely with the cork domain of FhuA.

Interactions between specific residues of FhuA and TonB are known to be highly conserved and may be essential for protein binding [30]. Electrostatic interactions are predicted between residue 166 in the C-terminal end of TonB, and residue 56 of the cork domain of FhuA. As such, residue 166 of TonB may act to disrupt the cork domain of FhuA [28]. This process would require energy derived from the PMF to induce structural change in TonB to disrupt the cork domain in FhuA and allow for passage of ferrichrome-iron across the OM and into the cell.

A fluorescent study also demonstrated TonB-FhuA interaction by labelling thiol-specific fluorophore N-[2-(1-maleimidyl) ethyl]-7-diethylaminocoumarin-3-carboxamide (MDCC) to the surface exposed region of FhuA [31]. Fluorescence quenching of 33% was observed when the hydroxamate-type siderophore ferricrocin was bound to FhuA, and 56% quenching when TonB was bound. Fluorescence spectroscopy further demonstrated that TonB is involved in promoting conformational changes to the surface exposed region of FhuA [31].

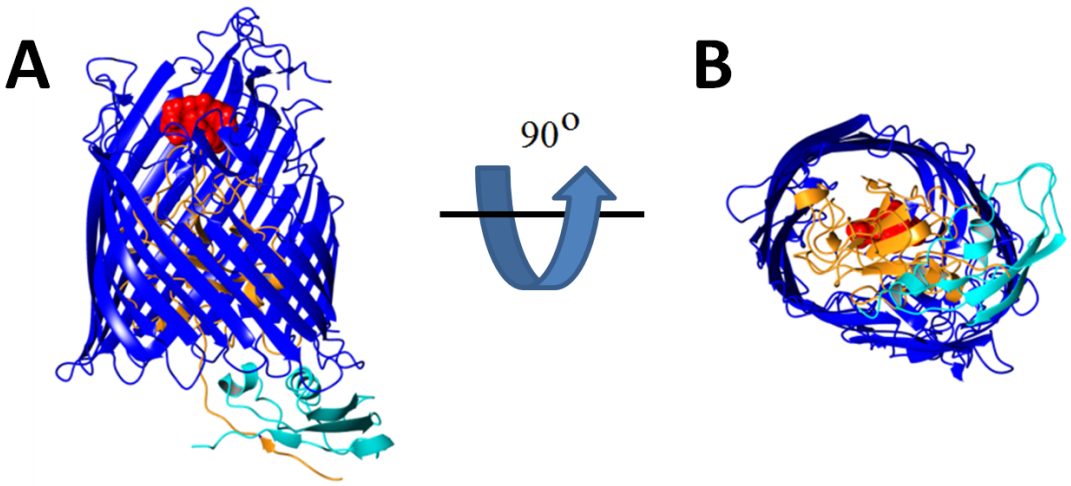

Figure 4. Crystal structure of the C-terminal domain of TonB bound to FhuA. TonB-FhuA complex resolved to 3.3 Å. Viewed from the OM plane is the hydroxamate-type siderophore ferricrocin (red) bound to FhuA (PDB code: 2GRX) (A). Interaction between the C-terminal domain of TonB (cyan) and the TonB box of FhuA, results in conformational changes to the FhuA cork domain (orange). A 90° orientation demonstrates FhuA's lumen viewed from the periplasm (B). The N-terminal switch helix has unwound 180° to provide FhuA-TonB interactions at the TonB box of FhuA, resulting in conformational changes to the cork domain.

1.3 Periplasmic binding proteins

Once nutrients have traversed the OM and into the periplasm, periplasmic binding proteins (PBP) capture the nutrients for transport to the CM. PBPs are typically divided into nine clusters based on their overall MW and by the chemical composition of their respective bound ligand [32]. For example, iron-siderophore and vitamin B_{12} transport across the periplasm is categorized as organic metal ion complexes, known as cluster eight.

Over 50 PBPs are reported for Gram-negative bacteria, with few homologues observed in the CM of Gram-positive bacteria. Although PBPs share a sequence identity of less than 10%, several crystal structures have been solved suggesting they are structurally conserved [33]. The crystal structures demonstrate PBPs as having two α-helical lobes, separated by an inner groove where the ligand can be bound.

Nutrients that have entered into the periplasm are delivered by PBPs to ATP-binding cassette (ABC) transporters embedded in the CM. ABCs are a large superfamily of nucleotide-binding proteins that assist in the transport of substrates across the CM, and are involved in DNA repair and RNA translation [34]. By binding and hydrolysing ATP at cytoplasmic subunits, ABC transporters harness this energy to transport substrates across the CM, once PBP-bound substrate comes into contact with the ABC transporter. ABC transporters not only uptake scarce nutrients from the periplasm and into the cytoplasm, but are

also involved in the transport of lipids, sterols, sugars, and metabolic products to and from the cytoplasm [35]. The interaction between PBPs and ABC transporters have thus far been shown *in vitro*; modeling of the PBP crystal structure for vitamin B_{12} transport in *E. coli*, BtuF, proposed bi-lobed folding when bound to ABC transporter BtuCD [36]. These results are similar to interactions between the PBP responsible for iron-siderophore transport in *E. coli*, FhuD, and the ABC transporter FhuBC [36].

Specific ABC transporters exist for the transport of iron-siderophore complexes and vitamin B_{12} from the periplasm to the cytoplasm. ABC transporters consist of four domains, two of which are transmembrane regions that comprise the substrate translocation channel; the remaining two domains are nucleotide binding domains responsible for the binding and hydrolysis of ATP. While overall structure of the ABC transporter for iron-siderophore, FhuBC of *E. coli*, remains unknown, it is known that the transmembrane region consists of a single polypeptide chain [37]. BtuC and BtuD proteins of *E. coli* interact in a 2:2 ratio to form the ABC transporter responsible for vitamin B_{12} transport [38]. BtuC consists of the two transmembrane regions with 10 transmembrane helices, and acts as the translocation channel. BtuD encompasses the nucleotide binding domains that are responsible to induce conformational changes to BtuC and allow for the substrate to enter into the cytoplasm [39]. Comparison of reported ABC transporter structures suggests that both the transmembrane domains and the nucleotide binding domains can either have a single or double

polypeptide chain. While no structure has been determined for the FhuBC complex, FpbC is an ABC transporter for ferric ions in *Neisseria gonorrhoeae,* and given its substrate specificity, may have structural similarities to the FhuBC complex [40]. The series of events proposed for the mechanism of ABC transporters entail binding of substrate, followed by nucleotide binding and ATP hydrolysis resulting in conformational changes in transmembrane domains; however, the overall interactions between domains remains largely unknown [41].

1.4 TonB-ExbB-ExbD complex

The mechanism by which iron-siderophores and nutrients larger than 600 Da are transported across the OM requires a readily available energy source. However, as there is no energy readily available at the OM or in the periplasm, energetic sources are derived from transmembrane ion potentials in the CM. TonB, ExbB and ExbD are three transmembrane proteins embedded in the CM that form a complex to provide energy necessary for TonB-dependent nutrient uptake. Energy obtained for this transport is derived from the PMF, which is a H^+ ion gradient maintained across the CM [42]. Energy harnessed by the ExbB-ExbD complex is proposed to transfer and extend TonB across the periplasm and interact with TonB-dependent receptors at the OM. As Gram-positive bacteria do not possess an OM, a recent study suggests that they also do not possess genes that encode TonB, ExbB or ExbD [43].

Analogous to the TonB system is the Tol system which contains three proteins, TolQ, TolR, and TolA, that interact similarly in the CM [44]. While TolQ and TolR are orthologues to ExbB and ExbD respectively, TolA is homologous to TonB. The Tol system is required for maintaining OM stability, and is present in several Gram-negative bacteria [45]. Similar to the TonB system, interactions between TolA and Pal lipoproteins at the OM require the use of the PMF [46]. While less is known about the TolA system compared to TonB-ExbB-ExbD, it has been proposed that the two systems share similar methods of harnessing the PMF. TolQ and TolR proteins are proposed to cause energy-dependent conformational changes to TolA for direct interactions with Pal lipoproteins [47]. A second system that shares sequence similarity and topology, with respect to the transmembrane regions of ExbB and ExbD, resides in the bacterial flagellar motor composed of MotA and MotB proteins respectively. ExbD contains four conserved residues in the transmembrane region with respect to MotB and TolR: Aspartic acid 23, Leucine 28, Leucine 29, and Phenylalanine 32 [48]. Given MotB and TolR homodimerize, these conserved residues may be potential structural determinants. Similar to the proposed role of ExbB and ExbD as an energy source, the transmembrane electrochemical gradient derived from a pore created by MotA and MotB provides the necessary energy source for generating torque to the flagella motor [49]. As MotA and MotB share sequence similarity in the transmembrane regions of ExbB and ExbD respectively, as well as TolQ and

TolR, studies in ExbB and ExbD may also provide further insight into these systems [48].

1.41 TonB

TonB of *E. coli* is 239 amino acids in length with an approximate MW of 26 kDa. TonB contains a single transmembrane region spanning the CM. The soluble N-terminal domain of TonB is an α-helix consisting of residues 1- 32, with residues 1- 12 occupying the cytoplasm, and residues 13-32 spanning across the CM (Fig. 5A). The N-terminal domain contains the hydrophobic signal sequence which is required for the translocation of TonB into the CM. The central domain located in the periplasm comprises residues 33-149 and forms an extended linker after the transmembrane region to the C-terminal domain. This linker is dominated by a proline rich region from residues 66-102 consisting of proline-leucine repeats. Currently the function of the proline-rich region is unknown, although studies confirmed that the removal of this region does not impede TonB from spanning the periplasm and interacting with TonB-dependent receptors at the OM [50]. However, recent developments suggest that the proline-rich region is required to obtain full interaction between TonB and FhuA [51]. The final domain of TonB is the C-terminal domain from residues 150-239. Only the C-terminal domain of TonB has been well defined by crystal structures solved for TonB of *E. coli* and TonB2 of *Vibrio anguillarum* [52].

High-resolution structures of the C-terminal periplasmic domain have been solved for varying lengths of TonB. The first structure of TonB, from residues 164-239, revealed a dimeric organization (Fig. 5B) [49]. This result was confirmed by analytical ultracentrifugation of the TonB-FhuA complex [53]. While the second C-terminal structure of TonB, from residues 150-239, again showed dimeric organization, further analysis demonstrated that the protein remained monomeric when in solution (Fig. 5C) [54]. The most recent construct of TonB, obtained by nuclear magnetic resonance (NMR), encompassed residues 103-239, and was the only construct that contained the entire C-terminal domain of TonB (Fig. 5D) [55]. Results demonstrated that the C-terminal domain of TonB was monomeric, as a β-hairpin in the C-terminal domain of TonB prevented dimer formation. Currently it is unknown whether TonB is monomeric or forms a dimer when in complex with ExbB and ExbD. TonB has been shown to interact with ExbB through *in vivo* formaldehyde cross-linking studies [56]. A further study demonstrated that the interaction between TonB and ExbB was dependent on residues Ser-16 and His-20 located in the transmembrane region of TonB [57]. Also, mutating the genes encoding for ExbB and ExbD resulted in a loss of approximately 90% of TonB-dependent activity.

Using phage display techniques, TonB-affinity selected peptides demonstrated interaction with PBPs, FhuD and BtuF, for the transport of iron-siderophore complexes and vitamin B_{12} respectively [58]. Further evidence of these interactions involved dynamic light scattering, which demonstrated TonB

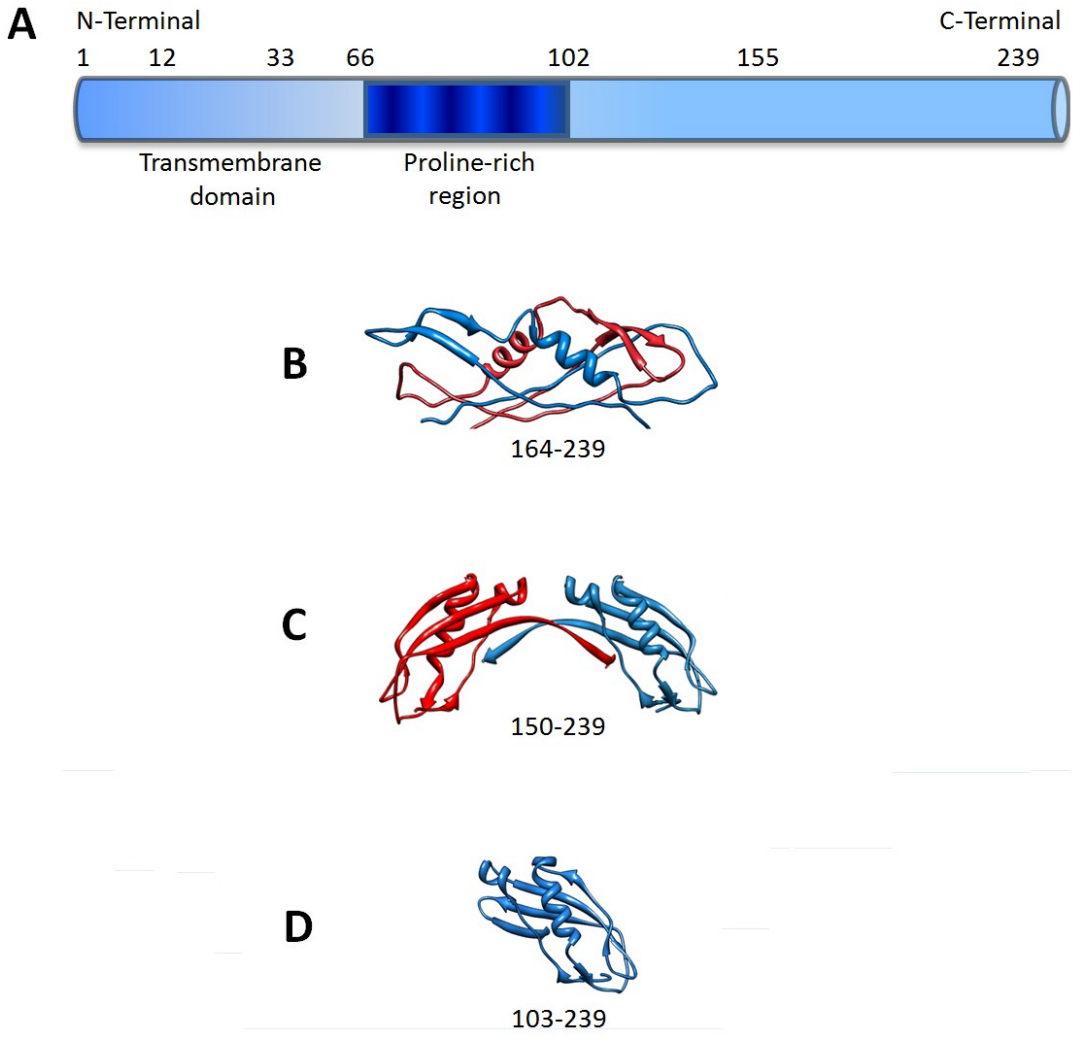

Figure 5: Topology of TonB and structures of the C-terminal domain. A representation of TonB's topology is demonstrated, with the single transmembrane domain near the N-terminal domain in the cytoplasm, and the proline-rich region (residues 66-102) and the C-terminal domain in the periplasm (A). Crystal structure resolved of the shortest TonB construct (residues 164-239) demonstrated dimeric organization; individual monomers are represented in red and blue (PDB code: 1QXX) (B). Second crystal structure (residues 150-239) also demonstrated dimeric organization, but was found to be monomeric in solution (PDB code: 1U07) (C). NMR structure of the C-terminal domain of TonB (residues 103-239) demonstrated monomeric organization (PDB code: 1XX3) (D).

and FhuD interact in a 1:1 complex [58]. By surface plasmon resonance, the addition of FhuD to a FhuA-TonB complex demonstrated a ternary complex, suggesting TonB acts to direct FhuD in the periplasm to accept the iron-siderophore for transport to the CM [58].

1.42 ExbB and ExbD

ExbB, the largest protein in the ExbB-ExbD-TonB complex, is 244 amino acids with a MW of approximately 26 kDa. The N-terminal end of ExbB resides in the periplasm, from residues 1-15, while the C-terminal end encompasses residues 196-244 in the cytoplasm. Unlike TonB, ExbB possesses three transmembrane helices with helix I spanning residues 16-39, helix II from 128-155, and helix III from 162-194 [59]. These findings were reinforced by bioinformatic predictions [60]. ExbB has been shown to interact with the N-terminal transmembrane helix of TonB, as exchanging this region with the CM transmembrane protein TetA to form a TetA-TonB hybrid, prevented formaldehyde cross-linking with ExbB [61]. Between transmembrane helices I and II of ExbB are residues 40-127, which occupy the cytoplasm, and may be required for interaction with other cytoplasmic proteins.

ExbD is the smallest protein of the complex at 141 amino acids with a MW of approximately 16 kDa. ExbD is topologically similar to TonB; the N-terminal end of ExbD is located in the cytoplasm from residues 1-22. ExbD also has a single transmembrane helix, from residues 23-42, and an extended

periplasmic domain from residues 43-141 [62]. High-resolution structure of the C-terminal domain of ExbD was solved by NMR (Fig. 6A) [63]. The structure is separated into three smaller domains and contains residues 44-141. The short periplasmic tail from residues 43-63 are disordered and likely a region of flexibility for ExbD. The larger domain from residues 64-133 demonstrated some stability in that it is composed of a single, five-stranded β-sheet between two α-helices. The C-terminal domain from residues 134-141 is also disordered. These results share structural similarity with the TolR homologue of *Haemophilus influenzae*, and the PBP for iron uptake, FhuD, as all three C-terminal domains demonstrate four mixed anti-parallel β-sheets between two α-helices (Fig. 6B and C) [64].

1.5 Proton pathway

Abundant energy is required for TonB-activity with TonB-dependent receptors at the OM. This energy is proposed to originate from ExbB and ExbD interacting together to harness the PMF H^+ gradient. With regards to the interactions between ExbB and ExbD, studies have demonstrated that ExbD co-purified with His_6-tagged ExbB via affinity column chromatography [64]. Another study demonstrated that bound ExbB prevented the degradation of ExbD [65]. *In vivo* formaldehyde cross-linking assays have also determined that ExbB and ExbD can form homomultimers [66].

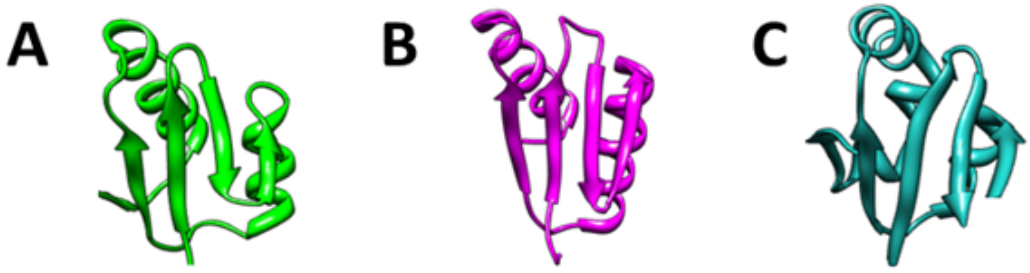

Figure 6. Homology of the C-terminal domain of ExbD by NMR. The C-terminal domain of ExbD demonstrates two α-helices flanking the four mixed anti-parallel β-sheet (PDB code: 2PFU) (A). Structural similarity is observed with an orthologue to ExbD, the TolR protein of *Haemophilus influenza* (PDB code: 2JWK) (B). The periplasmic binding protein FhuD, involved in the transport of iron across the periplasm, also shares homology with ExbD (PDB code: 1EFD) (C).

A mutagenesis study was attempted to identify critical residues facilitating the interactions between ExbB and ExbD and the proton pathway. Two residues, threonine 148 in helix II of ExbB, and T181 in helix III, are conserved in TolQ, and MotA; mutations to alanine resulted in loss of activity of these proteins [67]. A molecular modeling study on proton pathway function of ExbB and ExbD also included MotA and MotB as templates. The proton pathway proposed by this study requires function of helices II and III of ExbB, and transmembrane helix of ExbD. Therefore, studies have demonstrated that the binding of ExbD to ExbB is direct and not TonB-mediated [64].

1.6 Mechanism of action

Structural information for the membrane-spanning regions of TonB and ExbD, and all of ExbB remains unknown (Fig. 7). Furthermore, the stoichiometry and overall conformation of the TonB-ExbB-ExbD complex remain elusive. In an attempt to determine the stoichiometry of the complex, immunoblot strategies using purified ^{35}S-labelled proteins suggests that the TonB-ExbB-ExbD complex has a ratio in *E. coli* of 1:7:2 [68]. However, as it is currently unknown whether TonB forms a dimer, this ratio is not definitive of the actual stoichiometry. Furthermore, the structure of the most abundant protein, ExbB, remains unknown, complicating attempts to determine the overall mechanism of action of the TonB-ExbB-ExbD complex.

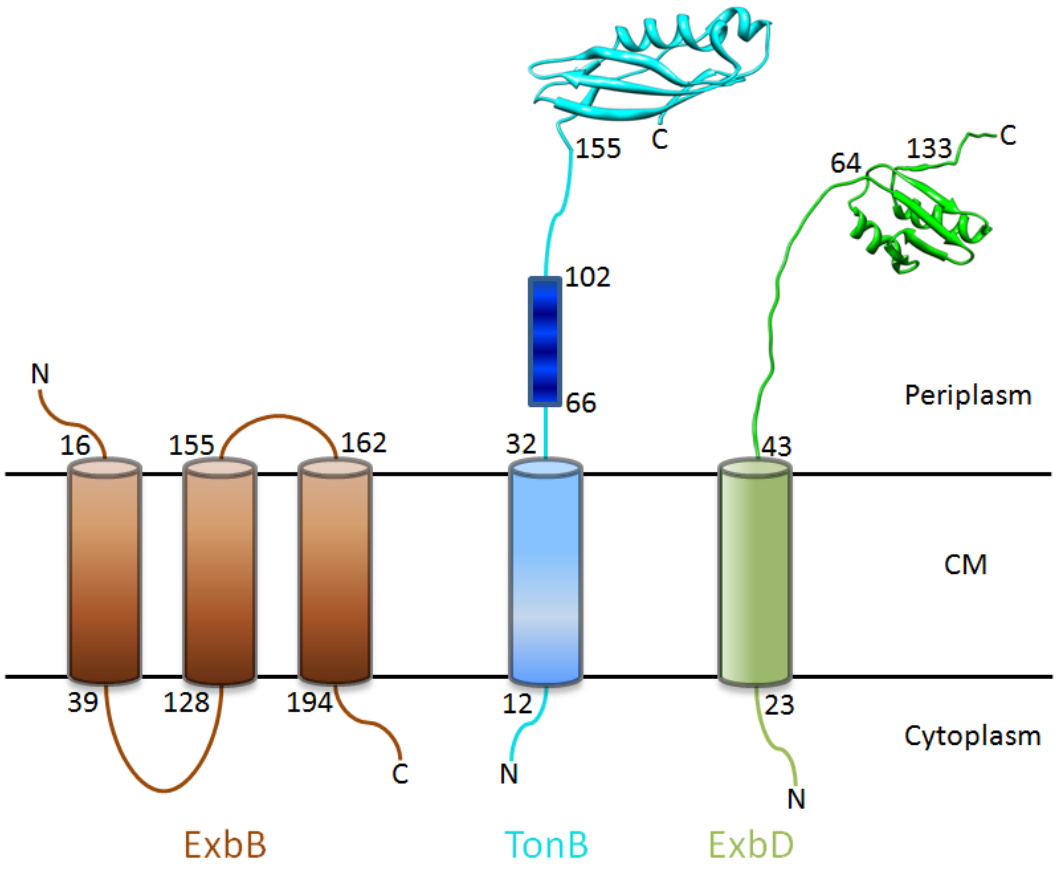

Figure 7: Topology of the TonB-ExbB-ExbD energy transduction complex. ExbB, proposed to be the scaffold protein of the complex spans the CM three times with an extended cytoplasmic region between helices I and II (brown). TonB (cyan) has a single transmembrane domain demonstrating the proline-rich region (residues 66-102) and the C-terminal domain structure as solved by NMR (residues 103-239) (PDB code: 1XX3). ExbD is topologically similar to TonB in that it has a single transmembrane domain, and demonstrated in the periplasm is the solved NMR structure of the C-terminal domain (residues 44-141) (PDB: 2PFU).

While the structural interactions between FhuA-TonB have been well documented as previously described, the molecular mechanism of proton translocation remains undetermined. Three methods have been proposed to describe TonB activity. The propeller model was based on the first crystal structure of TonB as a dimer [69]. This model proposes that the C-terminal domain of TonB dimerizes while remaining embedded in the CM to form a complex with ExbB and ExbD. Once ExbB and ExbD harness the PMF, a rotary motor similar to that of the MotA-MotB complex, would permit TonB to extend and interact with TonB-dependent receptors at the OM. However, one concern with this model is that there is no stationary platform to prevent ExbB and ExbD from rotating with TonB. This is in contrast to MotB whereby its C-terminal domain is anchored to the CM [70].

The shuttle model requires TonB to separate from the CM [71]. While TonB is pre-energized at the CM, ExbB and ExbD harness the PMF, thereby allowing energized TonB to separate from the CM, and bind to TonB-dependent receptors at the OM. TonB is proposed to transfer its energy to the OM receptor to transport substrate across the OM and into the periplasm. This model is based on *in vivo* labelling experiments that suggest the N-terminal domain of TonB is present in the periplasm during nutrient transport [72]. However, it is unclear how TonB would remove itself from the CM as this would be thermodynamically unfavourable given that the transmembrane region is hydrophobic. In addition, this model does not explain how TonB would retain its active conformation once

fully in the periplasm. Furthermore, it is unclear how TonB would return and imbed back into the CM after interaction with the OM receptor.

Single-molecule protein unfolding studies of other proteins suggest that the mechanism by which TonB interacts with the OM is achieved by a pulling method [73]. In this model, TonB remains embedded into the CM with ExbB and ExbD. Given that the plug domain of the TonB-dependent receptor and the C-terminal end of TonB are both four-stranded β-sheets, it has been proposed that when ExbB and ExbD harness the PMF, TonB spans the periplasm and actively pulls down the OM receptor via the TonB box. This would generate a channel in the OM large enough for the translocation of substrate. While TonB has been demonstrated to pull on the OM protein BtuB *in silico* [74], there are no *in vivo* experiments that support this proposed model.

1.7 Membrane protein over-expression and the role of detergents

Over-expression of recombinant proteins is necessary for the structural and functional study of proteins. *E. coli* is a model organism commonly used as an expression host given that its ease of manipulation and accessibility permits the incorporation of genes to express as proteins. Over-expression of a specific protein may yield milligram amounts that can be used for a wide-range of assays; however, there are limitations to over-expressing proteins. One concern is with regards to *E. coli* membrane chaperones which may become overwhelmed

during over-expression and result in protein misfolding [75]. Degradation, toxicity to the host cell and inclusion bodies may also disrupt over-expression of membrane proteins. Furthermore, membrane space may not be sufficient to contain over-expressed proteins, and may also cause over-expression of membrane proteins of non-interest [76]. Preventing these many factors in over-expressing membrane proteins in *E. coli* is maintained by working with the cultivated *E. coli* strain K-12 [75].

Following lysis of cells containing over-expressed proteins, and ultracentrifugation to obtain total membrane fractions, isolation of solubilized membrane proteins requires a stable solution maintained by detergents. Detergents, such as n-dodecyl-β-D-maltopyranoside (DDM), are structurally similar to that of lipids with a polar headgroup and a hydrophobic tail varying in length. Other detergents that can be used for membrane protein purification are n-decyl-β-D-decylmaltopyranoside (DM), and n-octyl-β-D-glucopyranoside (OG). When the concentration of detergent, such as DDM monomers, exceeds a certain limit, known as the critical micelle concentration, DDM monomers combine together to form micelles. The circular structure of micelles orients the polar headgroup to face the external solution, while the hydrophobic tails are maintained inside and away from the solution [77]. The interior of the micelle provides sufficient stability to allow intact solubilized membrane proteins to remain in solution and prevent association with external factors.

Fusing tags onto proteins of interest facilitates purification by chromatography and verification of protein expression by immunoblotting. Proteins fused with a His_6-tag are often purified to homogeneity using immobilized metal-affinity chromatography (IMAC). Use of a His_6-tag for purification is common given that its low MW prevents interference on the function and structure of fused proteins. As many proteins have intrinsic histidine or other features which may bind to the IMAC column and interfere with the protein of interest, binding, washing, and elution conditions must be optimized by varying imidazole concentrations. Imidazole is a substituent in histidine which permits the elution of bound proteins from the IMAC column by displacing the His_6-tag from the nickel ions. A second tag, in combination with His_6-tag, can fuse to the opposite terminus of the protein of interest. Glutathione S-transferase (GST), a globular 26 kDa protein, is a tag that increases the stability of fused proteins with a high binding affinity to glutathione ligands by Glutathione-Sepharose chromatography. Given its propensity to degrade, desirable is the inclusion of both GST and His_6 tags for the purpose of TonB purification.

1.8 Transmission electron microscopy

A transmission electron microscope (TEM) uses an electron beam for observing biological and inorganic specimens that would otherwise be too small to observe by light microscopy, or too large to solve by X-ray crystallization.

While non-confocal microscopes can achieve 2,000x magnification for 200 nm resolution, TEMs can reach upwards of 700,000x magnification. Increase in resolving power is provided by the electrons having wavelengths 100,000 times shorter than that of visible light [78]. When the electron beam is emitted from the electron gun, its acceleration is achieved by an electron current between 40 to 400 KeV. The electron beam is controlled and focused through the TEM by a set of electromagnetic lenses to provide interaction between charged electrons [79]. Each electromagnetic lens consists of a solenoid wire appended to a magnetic pole, whereby a current through the solenoid wire generates a magnetic field. This allows the electron beam to focus and produce a magnified image to record molecular structures less than 1 nm in diameter using a charge-coupled device (CCD) camera system [80].

While EM has been in existence since the 1930s, only recent technological advancements in EM have allowed for the determination of three-dimensional electron microscopy (3DEM) density maps of proteins. This is an advantage to X-ray crystallization given that the extended period of time to generate crystals is not required to achieve a resolution under 10 Å by electron microscopy (EM). The highest resolution attainable by cryo-EM is between 3.3 and 4.6 Å [81]. While this resolution is less than that of X-ray crystallization, the resulting 3DEM density map provides reliable atomic models for visualization. However, less than 20% of all structures submitted to the EM Data Bank (EMDB) have sub-10 Å resolution. Larger particles, such as viruses, require less data

collection by EM to obtain higher resolutions. This poses difficulty when attempting to obtain 3DEM density maps of proteins, given that their overall size is near the smallest scale to observe by EM. On average, protein complexes with a MW of 200 kDa are approximately 7.68 nm in diameter [82]. In comparison, spherical-virus particles, such as hepatitis C, have a diameter between 55 to 65 nm and many bacteriophages have an observed diameter of 25 to 35 nm [83].

There are many ways to prepare biological samples for EM. Use of EM carbon-coated copper grids is required to maintain the sample in a fixed position. Glow-discharging an EM grid prior to loading the sample converts the hydrophobic carbon-coat to hydrophilic [84]. This allows for proteins in solution to remain on the EM grid for further preparation. Chemical fixation by glutaraldehyde combined with formaldehyde, dehydration, and sectioning are all techniques predominantly used to analyze whole cells by EM [85]. Simple negative-stains such as uranyl acetate are used to observe molecular structures. Proteins in solution containing elements of a higher atomic weight, such as uranyl acetate, enhance the overall contrast to obtain clearer particles for data collection.

1.81 Preparation of micrographs by electron microscopy

State-of-the-art electron TEMs are available for the determination of molecular structures that include the FEI Tecnai T12 and FEI Tecnai G^2 F20. The

FEI Tecnai T12 has a voltage range between 20 and 120 KeV. Analysis of thin samples by the FEI Tecnai T12 can reach up to 700,000x magnification, and provides good spatial resolution for analytical techniques in both bright and dark-field imaging. The FEI Tecnai G^2 F20 is equipped with a field emission system for increased brightness, and provides a higher voltage electron beam at 200 KeV. This allows for finer analysis to obtain sub-nanometer spatial resolution [80].

High resolution EM can only be attained in a stable external environment. Temperature cooling panels are placed throughout the TEM room to maintain constant temperature of 20 °C. Room vibration and sound waves must be kept at a minimum to prevent shifting of the TEM which would otherwise decrease the resolution of the image. Correct alignment of the TEM is required for collecting high-quality micrographs. Astigmatisms can occur in many areas of the TEM including the objective lens, magnetic lens, resulting in chromatic and spherical aberrations [86]. Chromatic aberrations results in unfocused images caused by differences in the convergence points of all lenses. Spherical aberrations cause imperfect images when the refraction of the electron beam strikes an un-centered lens. Astigmatisms may disrupt the image generated resulting in an imperfect replica of the protein. For example, when the magnetic lens is not perfectly round, lens strength is distributed in two different directions. To alleviate this astigmatism, stigmators, defined as a device that adjusts magnetic lenses by generating a second magnetic field, introduce a magnetic quadrupole

lens to focus and deflect charged electrons [87]. This effect allows the electron beam to focus in a single direction to obtain a high-quality micrograph.

Collection of high-quality micrographs also requires the sample of interest to appear in focus through the ocular lens. There are two methods to determine the point of focus. The first method is manual analysis of carbon grains at two different points of contrast. Focus is achieved once a blank space is observed between the carbon grains. The second method is by Fast Fourier Transform (FFT). This mathematical operation in the TEM separates the image into constituent frequencies for analysis [88]. Focus is obtained when large concentric Thon rings, those that modulate the FFT of the image in a defocus-dependant way, are observed through a live feed of the CCD camera. Defocusing increases the distance between Thon rings to provide discernible concentric circles.

1.82 Image limitations by electron microscopy

Contrast limits the quality of biological samples collected by EM. Contrast is defined by the relative difference in intensity between an image point and its surroundings. In negative-staining EM, inherent contrast is weak due to proteins having atoms of lower atomic weight than uranyl acetate. Contrast can be increased by optimizing staining procedures and by taking into consideration the contrast transfer function (CTF). The CTF is the contrast of the image in all spatial frequency ranges [89]. This depends not only on spherical aberrations, but on

the level of focus of the objective lens. The CTF consists of two contrast factors: amplitude contrast, which is the scattering contrast from the electron beam resulting in loss of amplitude; and phase contrast, which is the interference contrast originating from shifts in relative phases of the electron beam to generate the image [89].

Radiation damage further limits the resolution of biological samples by EM. When radiation is too high, protein samples overheat from being bombarded by the electron beam. This causes molecular fragmentations resulting in loss of mass and potential molecular cross-linking [90]. The amount of energy in electrons required for analyzing protein samples by EM is between 100 and 300 KeV [91]. By increasing the energy of electrons, a higher-quality micrograph will be obtained; however, this will also increase radiation damage. Lowering the electron beam dose through low-dose techniques will result in a reduction in radiation damage. A low-dose strategy involves preparing and pre-calibrating the TEM to collect a micrograph in an area that does not contain protein sample. Once alignments are set, an image is collected at a site containing protein sample. Preparation away from the protein sample will prevent overexposure of the electron beam thereby reducing radiation damage [91].

1.83 Two-dimensional projections

Once micrographs are collected, EM image processing analysis is completed using computational software. Individual particles obtained from micrographs are boxed for analysis through a computational single-particle selection system (SIGNATURE) [92]. Recent advancements in particle picking programs have had success in reducing time allocation, and avoiding human interpretations of data. SIGNATURE normalizes the contrast of individually boxed particles to prevent bias selection based on the quality of the stain. The process described for the generation of two-dimensional (2D) projections were completed using computational single particle analysis for resolution extension (SPARX) [93]. The SPARX software suite was first used to properly align particles through the cross-correlation function (CCF). Alignment by CCF between two similar particles displays a high value, registering a motif that is contained in both images [94]. A 2D function of this motif is obtained when forming the cross-product of equivalent pixels as a function of the 2D vector.

Once particles are aligned by CCF, K-means classification differentiates individually boxed particles into designated K-subsets, where each subset is separated by their variance. A partition designates the center of each data set, where these new subsets generate novel centers of gravity. Data is then partitioned into stable 2D projections through several iterations of the maximum-likelihood (ML) multi-reference alignment method. This method

incorporates previously generated 2D classes as the starting template to obtain 2D projections of higher quality.

1.84 Three-dimensional reconstructions

To define 3DEM density maps, any dissimilarity between the experimental 3D image and 2D projections must be reduced. Using the SPARX software suite, 2D projections are used as a starting reference for generating an experimental 3D image. This involves particles from 2D projections aligning in 3D space. A 3D reconstruction is then further computed from experimental 3D images obtained from fixed alignment parameters. Once completed, the 3D volume is then projected as a new reference. Iterations reduce the discrepancy between 2D and 3D to improve alignment accuracy. Several iterations are required to obtain a high-resolution 3DEM density map.

1.85 Cryo-electron microscopy

Cryo-EM applies a higher dosage of electron beam to collect images, thereby increasing the overall quality of 3DEM density maps. By lowering the temperature of a prepared sample to temperatures below -180 ^{o}C, radiation damage is reduced by an order of magnitude. Given that the protein sample has not been stained, loss of information is less prevalent due to the sample being preserved in vitreous ice and not in contact with the EM grid. Furthermore, the

biological sample will remain hydrated in vitreous ice. This will prevent structural collapse of the biological sample and allows imaging at near liquid water conditions. As such, containing the sample in vitreous ice is beneficial for maintaining its near natural state. While the use of vitreous ice prevents preferential orientation of protein binding on the EM grid, electrons bombarding vitreous ice may vibrate and cause particles to shift resulting in reduced resolution [95].

Given the low signal to noise ratio, resolution from cryo-EM alone does not provide a 3DEM density map that can distinguish atomic features. Complementary studies by X-ray crystallization can provide crystal structures to dock into a 3DEM density map to potentially demonstrate new conformations.

1.9 Introduction to conducted research

Antibiotic-resistant pathogens are a leading cause of nosocomial infections. This includes pathogenic *E. coli*, which is the main causal agent of urinary tract infections. As such, discovery of additional antibiotic targets has become the primary research to combat Gram-negative pathogens. To reduce cross-resistance, novel targets that selectively inhibit bacterial growth are currently being considered. By focusing on the cell envelope of Gram-negative pathogens, development of novel antibiotics could block the uptake of scarce nutrients into the inner cell.

To develop these novel drug targets, further understanding of the TonB-ExbB-ExbD system is required. This system is a promising target given that their interacting receptors are essential in many Gram-negative pathogens, such as: *E. coli, Salmonella*, *Shigella,* and *Legionella* species [96]. By determining the overall conformation of the TonB-ExbB-ExbD complex, and identifying their stoichiometry, an understanding of the molecular mechanism of transport can be identified. By inhibiting the activity of the TonB-ExbB-ExbD complex, the uptake of these scarce nutrients would be inhibited and may reveal new antibiotic targets.

To understand the molecular structure and stoichiometry of the ExbB-ExbD complex that is proposed to harness the PMF, research by EM was pursued. These two proteins in the complex were chosen given that their direct interaction is independent of TonB. To investigate properties of ExbB-ExbD from *E. coli*, we expressed *exbB* and *exbD* together and *exbB* alone into vectors that appended His_6-tag fusions. After solubilisation in DDM, ExbB co-purified with His_6-tagged ExbD by IMAC, and purification by SEC identified a homogenous protein-detergent complex. Recombinant His_6-tagged ExbB was also expressed and purified by IMAC and SEC for comparative analysis. To elucidate the structural conformation of ExbB and ExbD in complex, the protein complex was analyzed by negative-staining EM. Single-particle analysis from high-resolution images was used to generate 2D projections of the ExbB-ExbD-His_6 complex. Comparison of the 3DEM density maps of ExbB-ExbD-His_6 and His_6-ExbB

suggested that the stoichiometry of ExbB and ExbD in complex is a ratio of 5:1-2 for ExbB:ExbD. Constructs containing various lengths of GST-tagged TonB expressed with ExbB-ExbD-His_6 were generated for future determination of the TonB-ExbB-ExbD complex by EM.

The hypothesis of my research project was that structural information obtained by EM for ExbB-ExbD-His_6 and His_6-ExbB, would provide further insight into the mechanism of energy-dependent nutrient import in bacteria.

Chapter 2 –Material and Methods

2.1 Bacterial strains and plasmids

E. coli M15 strain containing the commercially available pREP4 plasmid (QIAGEN) was obtained for the purpose of co-expressing wild-type ExbB and ExbD in complex with a His_6-tag appended to the C-terminal end of ExbD. pREP4 has a kanamycin-resistance marker, and expresses the lactose operon (*lacO*) for the purpose of a *lac*-inducible gene expression system. The ExbB-ExbD-His_6 complex was expressed using pExbBD derived from the commercially available pQE60 vector (QIAGEN) containing an ampicillin-resistance marker (Fig. 8). The *exbBD* operon of *E. coli* was cloned and inserted between NcoI and BamHI restriction sites in the multiple cloning site (MCS) of pQE60. The T5 promoter (T5p) regulates overexpression of ExbB-ExbD-His_6, and the lambda terminator controls transcription termination.

A second construct, pExbB, has a His_6-tag appended to the N-terminal end of ExbB alone, and was provided in May, 2005, by Christopher Koth, Ontario Center for Structural Proteomics, University of Toronto. His_6-ExbB was expressed in *E. coli* BL 21 DE3 strain containing the commercially available pLysS (QIAGEN), which has a kanamycin-resistance marker. *exbB* was cloned into a modified pET15b vector, where the thrombin cleavage site (LVPR^GS) was replaced with a tobacco etch virus (TEV) protease recognition site (ENLYFQ^G). *exbB* was cloned and inserted between NdeI and BamHI restriction sites of the MCS.

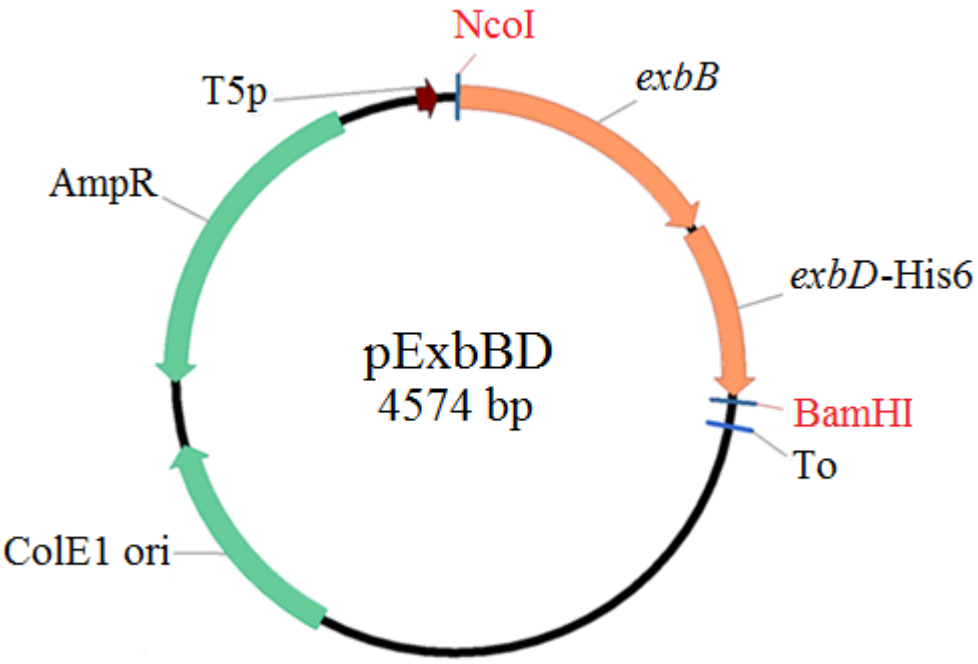

Figure 8. pExbBD. Wild-type *exbBD* operon containing *exbB* and *exbD* genes was inserted into the pQE60 vector (Qiagen) between restriction sites NcoI and BamHI. An ampicillin-resistance marker is incorporated into pExbB. T5 promoter regulates wild-type *exbBD* operon, and transcription termination is directed by the lambda terminator. A His_6-tag is appended to the C-terminal end of *exbD*.

Four more constructs were generated to co-express varying lengths of TonB with ExbB-ExbD. All *tonB* genes contained at minimum the N-terminal domain in the cytoplasm, and its single transmembrane domain. *tonB* genes varied as follows: N-terminal domain and transmembrane domain of *tonB* from 1-40 amino acids (a.a.) (pALC01 and pALC02); 1-66 a.a. of *tonB* (pALC03) extending into the periplasm prior to the proline-rich region; full-length *tonB* from 1-249 a.a. (Fig. 9). Each of the *tonB* genes were individually cloned into pExbBD. *tonB* has a GST-tag appended to the N-terminal region for stability and to prevent degradation. GST-*tonB* full-length insert was generated by Samuel Donato, former undergraduate honours student in Coulton Laboratory. Using the respective primers (Alpha DNA, Montreal), the GST-*tonB* insert provided by Samuel Donato was amplified by polymerase chain reaction (PCR). Digestion of pExbBD and appropriately designed primers GST-*tonB* insert was completed using Nco I and EcoR I restriction enzymes (Fermentas). On average, 300 ng of DNA was loaded to observe by 1% agarose gel electrophoresis, and resulting bands were excised by QIAquick Gel Extraction Kit (QIAGEN). DNA ligation was completed using DNA ligase (Invitrogen). Post-ligation species was transformed into XL-1 Blue *E. coli* cells; colonies were picked and grown in 5 ml LB, and mini-prepped (QIAGEN). Sequence fidelity of samples was confirmed by DNA sequencing (McGill University and Génome Québec Innovation Centre).

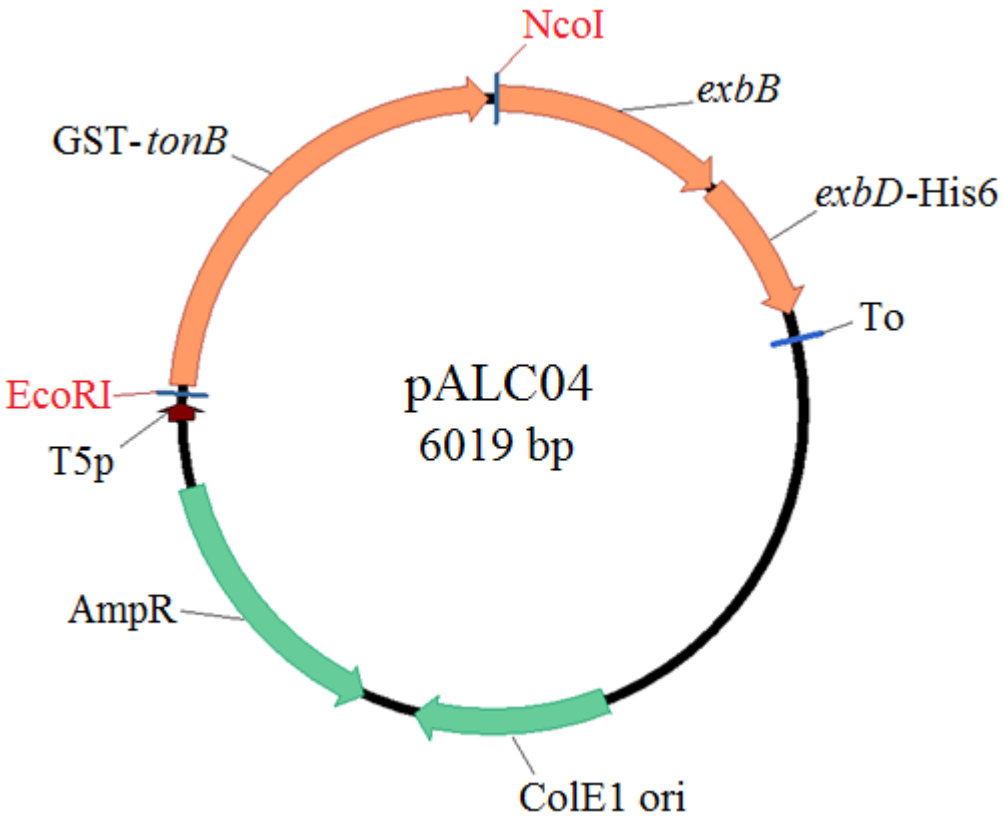

Figure 9. pALC04. Full-length *tonB* was inserted into pExbBD containing wild-type *exbBD* operon. The pALC04 construct also contains an ampicillin resistance gene as a selection marker. The *tonB* gene was cloned at the N-terminal end of the operon between EcoR I and Nco I restriction sites. N-terminal GST-tag was appended to *tonB* with a C-terminal His_6-tag appended to *exbD* for purification by Glutathione-Sepharose chromatography and Profinity IMAC respectively. Transcription termination is directed by the lambda terminator. Cloning strategy was similar for all pALC *tonB* constructs.

2.2 Protein expression

E.coli M15 pREP4 cells containing either pExbBD, or one of the pALC constructs containing a variation of GST-TonB with ExbB-ExbD-His_6, and *E. coli* BL 21 DE3 pLysS cells containing pExbB, were grown in Terrific Broth (TB) with 50 µg/ml ampicillin and 30 µg/ml kanamycin, 10% (v/v) glycerol, and 10% (w/v) of a mixture of monopotassium and dipotassium phosphates. Overnight pre-cultures in 25 ml of TB were used to inoculate 1 L cultures in Fernbach flasks. Cells were grown at 37 ^{o}C in a New Brunswick G-25 platform shaker until they reached an A_{600} of 1.0 to 1.2. Overexpression of the respective culture was induced by the addition of 0.4 mM isopropyl-β-D-1-thiogalactoside (IPTG) (Bio Vectra). Temperature was lowered to 24 ^{o}C by surrounding the Fernbach flasks with ice. Afterwards, the culture was left shaking for 4 hours at 24 ^{o}C. The cells were then collected by centrifugation at 5,000 rpm for 10 minutes at 4 ^{o}C (Sorvall H-6000 hanging bucket rotor). Harvested cells were frozen and stored at -20°C.

2.3 Protein purification

Cells harvested as previously described were re-suspended in lysis buffer (50 mM Tris pH 8.0, 200 mM NaCl) containing 5 mM $MgCl_2$, 100 µg/ml of DNAse I, 100 µg/ml of RNAse A, 10 µg/ml of lysozyme, and one tablet of mini-complete protease inhibitor cocktail (Roche). Re-suspended cells were lysed twice through an Emulsiflex homogenizer (Avestin) at 17,500 kPa. Centrifugation at 6,000 rpm

for 10 minutes at 4 ^{o}C (Sorvall SS-34 rotor) was completed to collect material of lysed cells in the supernatant. Total membrane fraction was obtained in the pellet following ultracentrifugation at 50,000 rpm for 1 hour at 4 °C (Beckmann Type 70.1 Ti rotor). Total membranes were solubilized overnight on a Thermolyne shaker at 4^{o}C in solubilization buffer (50 mM Tris pH 8.0, 150 mM NaCl and 1% (w/v) DDM with mini-complete protease inhibitor cocktail). Total membrane sample was then centrifuged for 45 minutes at 17,200 rpm (Sorvall SS-34 rotor) to collect the supernatant containing DDM-solubilized proteins for purification by Profinity IMAC or Glutathione-Sepharose chromatography.

Sample containing total membrane proteins was applied to a 1 ml Profinity IMAC column pre-equilibrated with 2 column volumes (CV) of equilibration buffer (50 mM Tris pH 8.0, 150 mM NaCl, 0.02% (w/v) DDM). Once the sample containing total membrane proteins was loaded onto the column, 10 CVs of wash buffer were applied (50 mM Tris pH 8.0, 150 mM NaCl, 0.02% (w/v) DDM, 35 mM imidazole). Ten CVs of elution buffer (25 mM Tris pH 8.0, 100 mM NaCl, 300 mM imidazole, and 0.02% (w/v) DDM) was applied to the column to remove bound material. After purification, protein concentration was determined using a bicinchoninic acid (BCA) kit (Pierce).

Total membrane sample containing one of the pALC constructs containing a variation of GST-TonB with ExbB-ExbD-His_6 was captured by Glutathione-Sepharose chromatography. DDM-solubilized proteins were applied to a 5 ml

Glutathione-Sepharose column pre-equilibrated with 2 CVs of equilibration buffer (20 mM Tris pH 8,0, 150 mM NaCl, 0.02% (w/v) DDM). Once the sample was loaded, the column was washed with 5 CVs of equilibration buffer. Five CVs of elution buffer (50 mM Tris pH 8.0, 150 mM NaCl, 0.02% DDM (w/v), 50 mM glutathione (GSH)) was applied to the column to remove bound material. Buffer exchange on the elution fractions to remove GSH was completed through several rounds of centrifugations of a 150 kDa MWCO concentrator (Pierce) at 3,750 rpm for10 minutes at 4 ^{o}C (Sorvall H-6000 hanging bucket rotor) . Protein concentration was then measured using the BCA kit (Pierce).

2.4 Western blotting

To detect expression of ExbB-ExbD-His_6 and His_6-ExbB, proteins were denatured and separated by SDS-PAGE. Protein bands were transferred onto an Immobilon-P Polyvinylidene fluoride (PVDF, Millipore) membrane overnight at 15 V with a Delta Electronik A power supply pack. The SDS-PAGE gel was then placed in Coomassie stain for 2 hours on an orbital shaker, and de-stained 3 times with de-staining solution (10% glacial acetic acid, 20% ethanol). Meanwhile, the membrane was blocked for 1 hour with 3% BSA in Tris-buffered saline (TBS, 50 mM Tris-HCl, 150 mM NaCl, pH 8.0). The membrane was rinsed with a TBS-0.05% Tween 20 (TBS-T) mixture and incubated on an orbital shaker for 1 hour in TBS with a 1/5,000 dilution of mouse α-His_6 IgG1 monoclonal antibodies (Clontech). Following incubation of the primary antibody, the

membrane was washed three times with TBS-T for two washes of 10 minutes each followed by one wash for 5 minutes. The membrane was incubated on an orbital shaker for 1 hour in TBS with a 1/10,000 dilution of goat α-mouse IgG alkaline-phosphatase conjugated antibody (Jackson ImmunoResearch). Following incubation of the secondary antibody, a second wash step with TBS-T was completed as described above. The membrane was then developed by incubating in TBS with a 1/50 dilution of Nitro blue tetrazolium chloride/5-Bromo-4- chloro-3-indolyl phosphate (NBT/BCIP) solution (Roche) in developing buffer (100 mM $NaHCO_3$, 1 mM $MgCl_2$) for 5 minutes. The NBT/BCIP reaction was stopped with distilled water.

For detection of GST encoded by the four pALC constructs that display variations of TonB with ExbB-ExbD-His_6, the membrane was incubated for 1 hour in TBS with a 1/5,000 dilution of mouse α-GST monoclonal antibody (Invitrogen). Following washing with TBS-T as described above, the membrane was incubated for 1 hour in TBS with a 10,000 dilution of horse radish peroxidase conjugated rabbit anti-mouse IgG2b antibody (Invitrogen). Following the second washing step with TBS-T, the membrane was developed with 20 mg of 3,3'-diaminobenzidine tetrahydrochloride hydrate (Sigma-Aldrich), 30 mL TBS pH 7.6, and 24 µl H_2O_2 for 10 minutes.

For detection of full-length TonB in pALC04, the membrane was incubated for 1 hour in TBS with a 1/5,000 dilution of anti-*Trypanosoma brucei*

procyclin monoclonal antibody. This detects for the proline-glutamic acid repeats in the proline rich region of TonB from 70-77 a.a. Following washing with TBST-T as described above, the membrane was incubated for 1 hour in TBS with a 1/5,000 dilution of goat anti-mouse IgG alkaline-phosphatase conjugated antibody (Jackson ImmunoResearch). Following the second washing step with TBS-T, the membrane was developed by incubating in TBS with a 1/50 dilution of NBT/BCIP solution (Roche) in developing buffer (100 mM $NaHCO_3$, 1 mM $MgCl_2$) for 5 minutes.

2.5 Size-exclusion chromatography

Following purification by Profinity IMAC, SEC was performed separately on ExbB-ExbD-His_6 and His_6-ExbB to assess homogeneity. A 26ml (10mm x 300mm GL) Superose 6 (GE Healthcare) column was pre-equilibrated with 2 CVs of equilibration buffer (25 mM glycine pH 9.0, 100 mM NaCl, and 0.02% DDM). A volume of 500 µl, containing approximately 100 µg of purified protein, was injected onto the column. Proteins were separated and eluted by applying a constant flow rate of 0.5 ml per minute of equilibration buffer to the column. The MW of the protein sample was determined by comparing the elution volume to a calibration curve of soluble proteins with known MW.

2.6 Negative-staining electron microscopy

Purified ExbB-ExbD-His_6 and His_6-ExbB collected by Profinity IMAC were dialyzed overnight to remove imidazole using a 25 kDa nominal MW cut-off (NMWCO) membrane in 25 µL dialysis buttons with dialysis buffer (25 mM Tris pH 8.0, 100 mM NaCl, and 0.02% DDM). The dialyzed sample was diluted to an optimized protein concentration of 6 µg/ml. Five µl of sample containing either ExbB-ExbD-His_6 or His_6-ExbB was applied to glow-charged carbon-coated EM copper grids and incubated for 1 minute. The protein sample was then blotted and 5 µl of 2% (w/v) uranyl acetate was added for 1 minute and then blotted. Initial micrographs for the determination of protein concentration optimization were obtained using the FEI Tecnai T12 (105,000x to 165,000x magnification), and micrographs for data collection were obtained in low-dose conditions on the FEI Tecnai G^2 F20 (50,000x magnification) recorded on a Gatan Ultrascan 4k x 4k Digital CCD Camera System.

Eucentric height alignment in the TEM is required for obtaining high-quality images. Eucentric height can be set by configuring the tilt axis until it coincides with the object plane. This is achieved by rotating the sample holder apparatus of the TEM to $+60^o$ using the Alpha wobbler mechanism in the TEM, followed by adjusting the z-height and then rotating to -60^o, providing translation along the tilt axis.

2.7 Low-dose electron microscopy and contrast transfer function correction

High-quality micrographs for data collection are obtained through low-dose conditions on the FEI Tecnai G^2 F20. To reduce the bombardment of electrons onto the protein sample, pre-calibration of the TEM is performed in an area that does not contain protein sample. Once these alignments are completed, an image is collected at a site with protein sample. When collecting micrographs, adjusting for the contrast transfer function (CTF) parameter fitting is necessary as this directly affects the contrast of the image for all spatial frequency ranges. As such, the only varying parameter for collecting a micrograph in low-dose EM conditions is adjusting defocus. Varying defocus will enhance different features of the particles given that the CTF oscillates from -1 to 1, where the zero crossing does not exhibit contrast. To correct for this loss of information, 20 micrographs are taken at 0.2 µm defocus intervals. Due to their differences in signal to noise ratio, for negative-staining EM, defocus is set between -1.5 to -2.5 µm; for cryo-EM, defocus is set between -2.5 to -3.5 µm. CTF correction is then performed when classifying particles into their respective 2D class averages.

2.8 Cryo-electron microscopy

Preparations of ExbB-ExbD-His_6 were dialyzed following purification by Profinity IMAC as previously described. ExbB-ExbD-His_6 was diluted to an optimized protein concentration of 120 μg/ml for cryo-EM. Reproducible preparations of ExbB-ExbD-His_6 onto C-flat cryo-EM grids possessing 2 μm wells (Quantifoil) were achieved by a Vitrobot Mark IV (FEI) automated vitrification robot. Conditions were set at 4°C and 100% humidity to prevent condensation. ExbB-ExbD-His_6 was applied to the cryo-EM grid and automatically blotted for an optimal 25 second blotting time. The cryo-EM grid was then automatically plunged into liquid ethane at -150 °C. Afterwards, ExbB-ExbD-His_6 is contained in vitrified ice by manually transferring the cryo-EM grid into a cryo-EM grid box that is submerged in liquid nitrogen at -180 °C for long term storage.

Using the FEI Tecnai G^2 F20, low-dose techniques were applied to collect micrographs with a reduced intensity of 20 $e^-/Å^2$ per every one second of exposure. Given vitrified ice formation varies in height for every individual well on a cryo-EM grid, an image was first collected in search mode at 1,500x magnification. Ice thickness can then be measured using available computer software from the TEM, and select images were acquired at 50,000x magnification in wells projected to have very thin ice. Only one micrograph was acquired per well in a cryo-EM grid to prevent data collection at prior exposed sites.

2.9 SIGNATURE: computational single-particle selection system

Once micrographs were collected using low-dose techniques on the FEI Tecnai G^2 F20, EM image processing analysis was performed using computational software (Fig. 10). Individual particles were boxed and separated through the computational software SIGNATURE [92]. To automatically collect particles of ExbB-ExbD-His_6 or His_6-ExbB, a template was generated by first manually collecting 2,000 particles. A template with six classes was generated based on the orientation of particles when imaged. Manual collection of particles was performed when particles were not automatically boxed using the templates in SIGNATURE. Contrast in individually boxed particles was normalized to prevent computational bias selection. The SPARX software suite performed rotational and translational alignment of boxed particles and centered each particle through the CCF prior to 2D analysis.

2.10 Two-dimensional class averaging

K-means classification, a computational method for cluster analysis, was performed on all boxed particles using the SPARX software suite [93]. K-means classification allows particles that are in similar orientation to be clustered into a single class average. Several rounds of iterations are required to obtain 2D projections with distinct features. On average, each class contains the same amount of particles. Further optimization can be achieved by running several

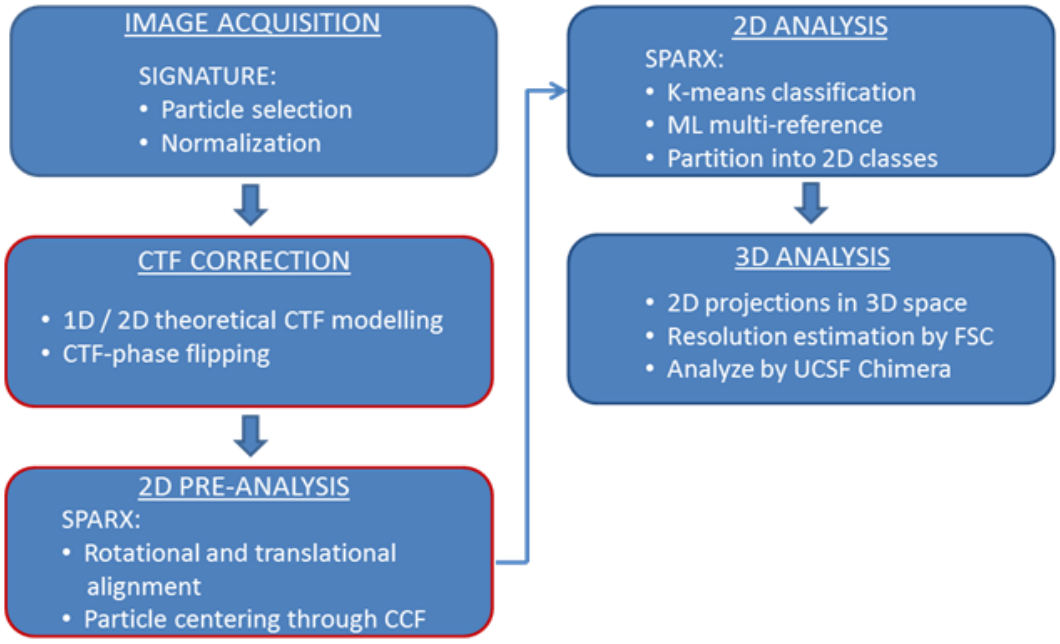

Figure 10. Schematic workflow of electron microscopy image processing analysis. Particles were individually boxed and normalized in SIGNATURE. Intermediary steps using the SPARX software suite prior to 2D data analysis are denoted in red outlines. K-means classification and maximum-likelihood multi-referencing using the SPARX software suite further refined 2D projections. 3DEM density maps were generated using the SPARX software suite by projecting 2D classes in 3D space. Resolution was resolved by FSC and 3DEM density maps analyzed by UCSF Chimera software.

rounds of the maximum-likelihood (ML) multi-reference alignment method using the SPARX software suite [97]. This process uses class averages previously obtained through K-means classification as a template to re-classify boxed particles for higher quality 2D projections.

2.11 Three-dimensional electron microscopy density maps

3DEM density maps were generated from a subset of 300 2D class averages. 3D structure determination requires several iterations using the SPARX software suite to converge 2D projections into 3D space. Resolution of a 3DEM density map uses the Fourier shell correlation (FSC) to measure the cross-correlation coefficient between two 3D volumes [98]. This is achieved by splitting the entire data set into two sub-sets, defined as the even-odd test. A computation is calculated to determine the resolution at 0.5 FSC between the two 3D volumes over frequencies in 3D space [98]. Interactive visualization and analysis of the 3DEM density maps were performed through UCSF Chimera [99].

Chapter 3: Results

3.1 Purification of ExbB-ExbD-His_6

E. coli cells containing pExbBD were grown as described in Section 2.2. Addition of DDM was required to lower the overall surface tension of the protein complex, resulting in the formation of a protein detergent complex (PDC). Purification by Profinity IMAC was completed using the His_6-tag appended to the C-terminal end of ExbD (Fig. 11). To purify the ExbB-ExbD-His_6 complex, proteins were captured by the His_6-tag bound to the Ni^{2+}-resin when the sample was loaded onto the column. As the His_6-tag was only appended to the C-terminal end of ExbD, any presence of ExbB following purification suggested ExbB co-purified with ExbD. Proteins of non-interest that did not have an affinity to metal were eluted in the flow-through and were completely removed during the wash step containing 35 mM of imidazole. Afterwards, 300 mM of imidazole was added to the column to act as a competitor and remove bound His_6-tagged ExbD. To obtain the greatest yield and purity of the ExbB-ExbD complex, the elution buffer following purification consisted of 25 mM Tris pH 8.0, 100 mM NaCl,300 mM of imidazole and 0.02% DDM.

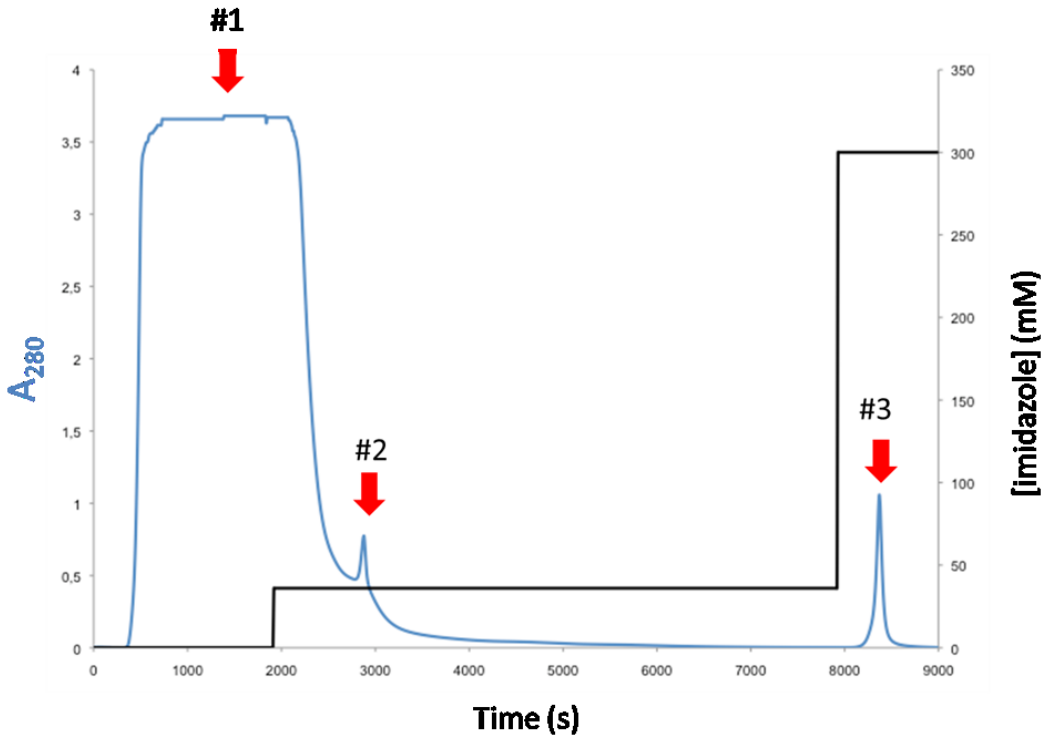

Figure 11. Chromatogram demonstrating purification of ExbB-ExbD-His_6 by Profinity IMAC. Solubilized total membranes containing ExbB-ExbD-His_6 were applied onto the Profinity IMAC column to capture the ExbB-ExbD-His_6 complex. Proteins of non-interest that do not have an affinity towards the Ni^{2+}-resin were removed from the column, represented by the flow-through (#1). A wash step containing 35 mM imidazole removed loosely bound proteins that have a low affinity to the Ni^{+}-resin (#2). Elution fractions were obtained with the addition of 300 mM Imidazole, and the elution peak containing ExbB-ExbD-His_6 was collected (#3).

From consistent purified preparations by Profinity IMAC, elution fractions proposed to contain the ExbB-ExbD-His_6 complex were analyzed by SDS-PAGE stained by Coomassie, or silver, and by α-His_6 Western blotting. By silver stain, two prominent bands were detected from elution fractions following purification by Profinity IMAC (Fig. 12). The upper protein band, at approximately 26 kDa, denoted the expected migration of ExbB, while ExbD was observed at approximately 16 kDa. It is important to note that when analyzing the quality of purified samples stained by either Coomassie or silver, the thickness of the bands on the respective gel does not correlate with the amount of total protein that was purified. From results obtained by silver stain, ExbB appeared to co-purify with ExbD-His_6.

Western blot analysis confirmed the presence of ExbD given its C-terminal His_6-tag (Fig. 12). Analysis of several purified preparations by Western blot detected only a single band at approximately 16 kDa, denoting ExbD-His_6 was present in the complex. No band was observed at 26 kDa; the band observed at that position on the silver stain was ExbB, demonstrating that ExbB and ExbD purified in complex.

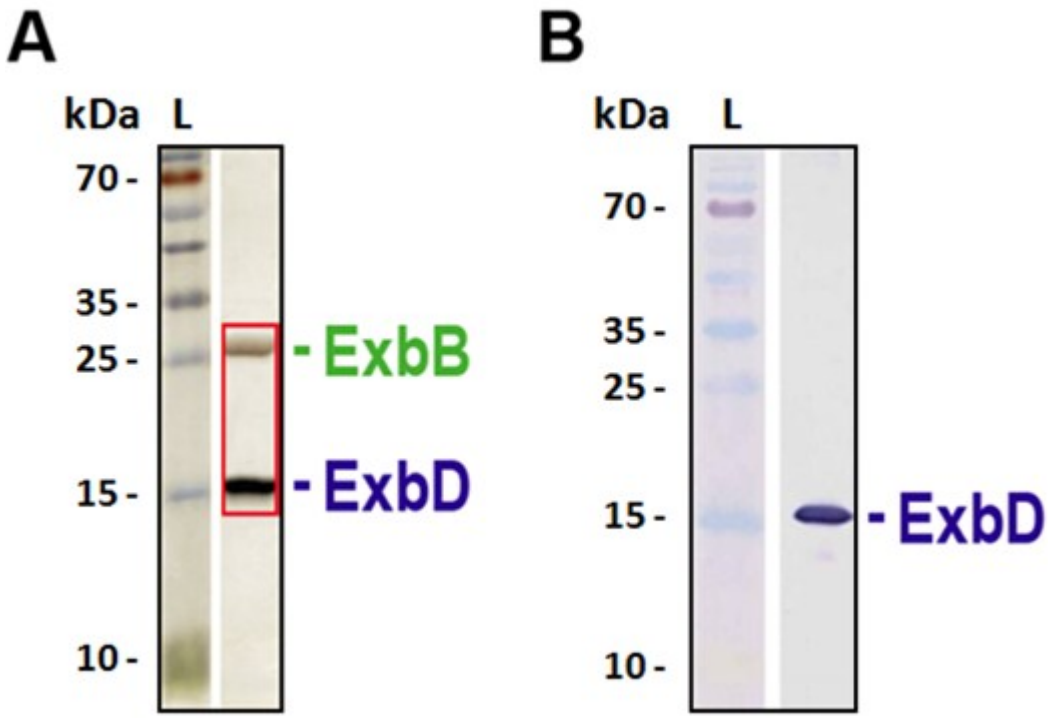

Figure 12. Quality of the purified ExbB-ExbD-His_6 complex. Elution fractions from purification by Profinity IMAC were analyzed by silver stain (A) to assess content and purity of the samples. Two prominent bands were observed denoting ExbB and ExbD. As the His_6-tag was appended to the C-terminal end of ExbD, only ExbD was observed in the western blot probed with α-His_6 antibody (B). L: MW ladder.

An extra purification step provided insight into complex formation of ExbB-ExbD-His_6. SEC elucidated whether the complex was homogenous, in addition to measuring the approximate MW of the ExbB-ExbD-His_6 complex (Fig. 13). Results obtained by SEC demonstrated a single symmetrical peak for the ExbB-ExbD-His_6 complex.

Results by SEC suggested that the formation of the complex was homogenous. By comparing elution time against calibrated standards of soluble proteins, the molecular mass of the ExbB-ExbD-His_6 complex was estimated at approximately 350 kDa. However, considering the effects of adding DDM to the ExbB-ExbD-His6 preparation, 350 kDa was proposed to be an overestimate of the true MW of the protein complex [100].

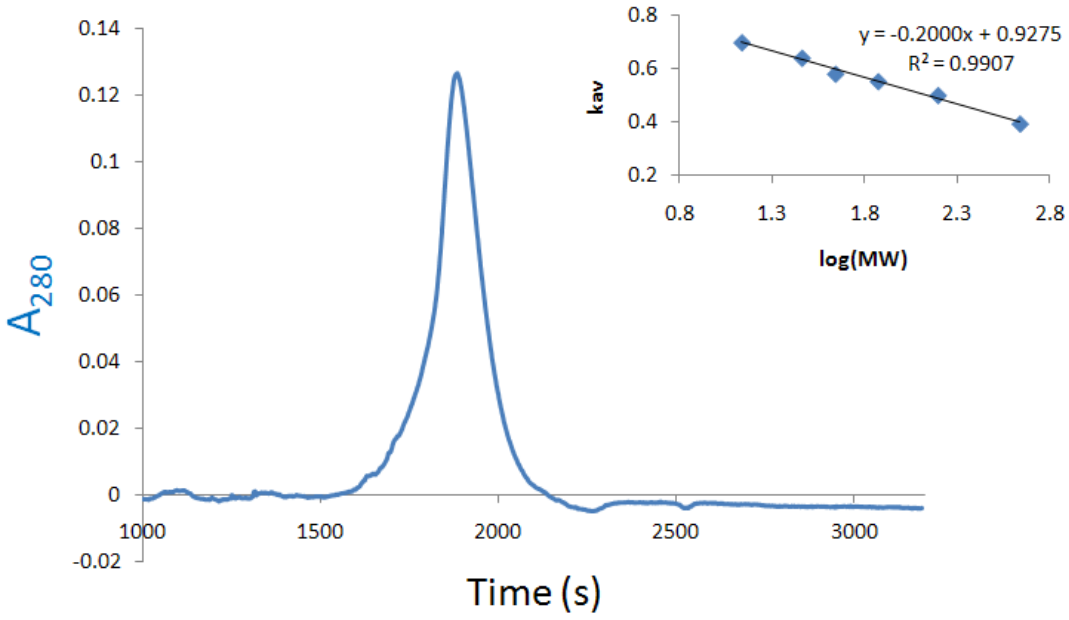

Figure 13. Chromatogram demonstrating the ExbB–ExbD-His$_6$ complex by SEC. Elution fractions from Profinity IMAC containing purified ExbB-ExbD-His$_6$ was loaded onto a Superose 6 column and assessed by SEC. The presence of a single symmetrical peak suggested a homogenous sample of ExbB-ExbD-His$_6$. The MW of the complex, estimated at 350 kDa, was determined by using the calibration curve prepared for the Superose 6 column from known soluble proteins (upper-right panel).

3.2 Negative-staining electron microscopy of ExbB-ExbD-His_6

Following consistent purified preparations of the ExbB-ExbD-His_6 complex by Profinity IMAC as noted in Section 3.1, samples were prepared for analysis by negative-staining EM. First, the high concentration of imidazole in elution fractions containing purified proteins had to be removed as this competing molecule created an impenetrable coat across the EM grid. Therefore, overnight dialysis through a 25 kDa NMWCO membrane in 25 µl dialysis buttons was required to have a purified sample in a solution containing 25 mM Tris pH 8.0, 100 mM NaCl, and 0.02% DDM. Preparation of purified sample for negative-staining EM involved placing the sample onto glow-discharged, carbon-coated EM grids, followed by the addition 2% (w/v) uranyl acetate used to stabilize the sample onto the EM grids.

When first preparing samples onto EM grids, a dilution series was made to determine the optimal concentration for analysis of ExbB-ExbD-His_6. Optimal concentration was demonstrated by obtaining particles that were not only separated for individual analysis, but by also maintaining a high concentration so that many particles can be collected per micrograph. Dilutions ranged from the initial concentration of 760 ng/µl of the dialyzed purified sample, to 1/256 (3 ng/µl). The optimal dilution determined for the ExbB-ExbD complex was 6 ng/µl.

Initial analysis of ExbB-ExbD-His_6 by negative-staining EM was performed on the FEI Tecnai T12 TEM; although the quality of its CCD camera does not allow

data acquisition for generation of 3DEM density maps. The FEI Tecnai T12 can be used to observe particle homogeneity, as well as their approximate diameter. Micrographs were collected at 135,000x and 160,000x magnification with defocus set to 1.5 µm.

Initial observations of ExbB-ExbD-His_6 using the FEI Tecnai T12 suggested particles were approximately 10 nm in diameter; this was later confirmed using a measurement tool provided in tilt tomography software on the FEI Tecnai G^2 F20. Particles appeared largely homogeneous on the EM grid, with various orientations depending on their position when originally stabilized onto the EM grid. This was the preferred result, as different angles of particles generate a more accurate 3DEM density map.

3.3 Data acquisition in low-dose by negative-staining electron microscopy

Once initial observations using the FEI Tecnai T12 confirmed a homogeneous sample of ExbB-ExbD-His_6 on the EM grid, data acquisition of particles using the FEI Tecnai G^2 F20 was pursued. The FEI Tecnai G^2 F20 can operate under low-dose conditions, as described in section 2.6, to prevent overexposure of the electron beam from causing radiation damage to the sample. Areas of possible interest on the EM grid containing ExbB-ExbD-His_6 were first examined at 1,500x magnification. Micrographs acquired by low-dose EM on the

FEI Tecnai G^2 F20 were exposed at 50,000x magnification (Fig. 14A). A total of 45,321 particles were collected from 131 micrographs for the ExbB-ExbD-His_6 complex by negative-staining EM.

3.4 SIGNATURE: boxing individual particles of ExbB-ExbD-His_6

Once all particles were collected, data analysis followed with the use of SIGNATURE, a computational single-particle selection system [92]. Each micrograph contained approximately 390 particles of the ExbB-ExbD-His_6 complex. To analyze particles obtained by the FEI Tecnai G^2 F20, SIGNATURE was used to individually box each particle for 2D classification.

A template of ExbB-ExbD-His_6, constructed from manually picking 2,000 individual particles, was generated for automated picking. Six distinct class averages based on various orientations of ExbB-ExbD-His_6 particles were obtained. Four classes that were considered to best represent the ExbB-ExbD-His_6 particles were used as a template to collect the remaining 43,321 particles. While SIGNATURE used the four class averages as a template to automatically collect particles on a micrograph, any remaining particles that were missed by the software were then manually collected. Afterwards, all individually boxed particles were normalized for comparison. Particles were deleted when they were not centered in their respective box, or when there was more than one

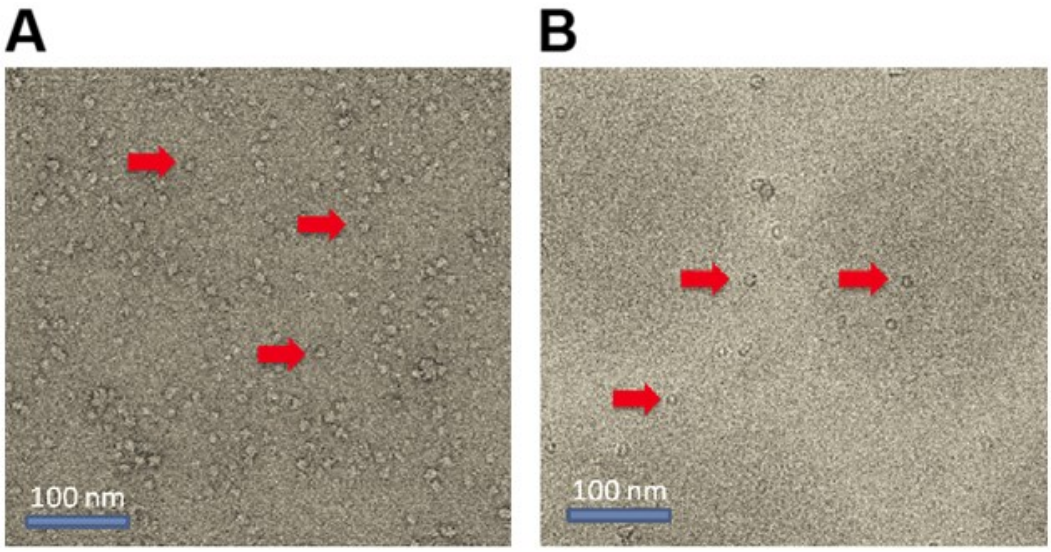

Figure 14. Electron microscopy of the ExbB–ExbD-His$_6$ complex. Post-IMAC ExbB-ExbD-His$_6$ samples were deposited onto glow-discharged carbon-coated EM grids. Proteins were stained with 2% uranyl acetate and then observed with a FEI Tecnai G^2 F20 TEM. Micrographs were collected at 50,000x magnification and CTF (contrast transfer function) corrected. (A) Representative EM micrograph of negatively-stained ExbB-ExbD-His$_6$ complexes. (B) Preliminary observations of ExbB-ExbD-His$_6$ by cryo-EM extended findings obtained by negative-staining EM.

particle in any given box. This enabled a more accurate classification of particles for 2D averaging.

3.5 SPARX: Computational single particle analysis for resolution extension

Although all 45,321 particles were individually boxed, they still remained separated by their respective micrograph. Prior to generating 2D projections of ExbB-ExbD-His_6, all particles were stacked into a single file to analyze as a whole. K-means classification of the set of images was then performed using the SPARX software suite for computational single particle analysis. K-means classification distinguished particles that were in similar orientation to be clustered into a single class average. Several rounds of iterations through exhaustive search algorithms were required to obtain 2D projections with distinct features. To begin, six class averages were generated from eight iterations of K-means classification; however, given the low number of class averages, particles that only shared relative orientations were forced into the same class. Therefore, on average, each class contained approximately 7,500 particles.

Once the first six class averages were generated, these classes were partitioned into the maximum-likelihood (ML) multi-reference alignment method to obtain more accurate 2D projections [97]. All particles were centered using CCF prior to analysis to increase the accuracy of multi-reference alignment. Specifications in the SPARX software suite allowed the classification to be based

on the inner and outer radii of particles for rotational correlation. Considering all individually boxed particles are not aligned, a translational alignment procedure uses an algorithm to determine the range in both the X and Y directions. When first beginning multi-reference alignment, the translational alignment was unknown and was therefore set to zero, which was the equivalent of the rotational alignment. Once the first several iterations of K-means classification was completed, the translational alignment was determined for ExbB-ExbD-His_6 at an arbitrary value of six. This allowed for all individually boxed particles to be properly aligned for 2D reconstruction.

Following the generation of the six class averages, further optimization was obtained by creating eight class averages, which were then further optimized into twelve classes, followed by 28 and finally 64 classes through the assistance of the ML multi-reference alignment method. Each round of classification had an increase in the amount of iterations with the highest being 30 rounds for the 64 classes. When 28 classes were generated, classes for ExbB-ExbD-His_6 that had fewer than 300 particles were deleted. 2D projections were then generated from the 64 classes into a set of 12 2D projections (Fig. 15). All class averages, each containing approximately 3,800 particles, appeared to be the same homogeneous complex with variations in orientation. No symmetry was imposed for the ExbB-ExbD-His_6 complex. In Figure 15, the class average boxed in red illustrates the frontal symmetry of the complex as it would appear when observing the CM from either the periplasm or cytoplasm.

Figure 15. 2D projections of ExbB-ExbD-His$_6$ in complex by negative-staining EM. Individually boxed particles (45,321) were aligned and classified for similarity using the ML multi-reference alignment methods. Each average (or class) contained approximately 3,800 particles. Differences between class averages demonstrate varying orientations of ExbB-ExbD-His$_6$. Illustrated in the red box denotes ExbB-ExbD-His$_6$ at a proposed orientation of either 90° above or below the CM plane.

Analysis of the 2D projections suggested a symmetrical pentameric organization for ExbB-ExbD-His_6 complex. The 2D projections allowed for the generation of a 3DEM density map. Several rounds of computational operations using the SPARX software suite created a 3DEM density map from a subset of 300 class averages of the ExbB-ExbD-His_6 complex. By measuring the normalised cross-correlation coefficient between two 3D volumes as a function over corresponding shells in Fourier space, ExbB-ExbD-His_6 complex was resolved to a resolution of 22.5 Å (Fig. 16). Analysis of the 22.5 Å 3DEM density map confirmed a pentameric organization of ExbB in the ExbB-ExbD complex, with each ExbB subunit having a measured height of approximately 8 nm. As ExbB is a transmembrane protein, the height of these subunits would be sufficient to span across the CM with its reported thickness of approximately 7.5 nm [101]. A difference in quality of one of the five ExbB subunits (Fig. 16) is common in negative-staining EM due to particles having favourable binding to the carbon-coated EM grids.

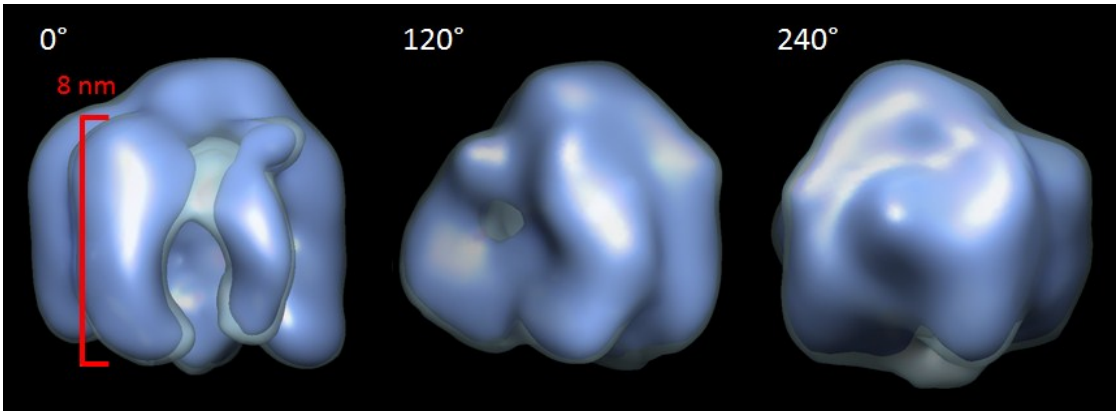

Figure 16. 3DEM density map of ExbB-ExbD in complex by negative-staining EM. The 3DEM density map was calculated using the SPARX software suite from 45,321 particles and reached a resolution of ~22 Å. The map contains five elongated densities ~8 nm in height as observed at 0° and 120°. Each density could correspond to one ExbB subunit. ExbD is proposed to be located in the upper region of the 3DEM map observed at 240°. The proposed stoichiometry is five ExbBs and one or two ExbDs in the complex.

Based on its extended periplasmic region, ExbD is proposed to be located in an extension of increasing density in the cross-section of the upper region of the 3DEM map (Fig. 17). Currently unknown is whether there is a monomer or dimer of ExbD within the complex. If a dimer of ExbD exists in the complex, the sole area of density not attributed to ExbB in the 3DEM density map projects that the two ExbD subunits would be in the same location and exhibit possible interactions with each other within the complex.

3.6 Cryo- electron microscopy of ExbB-ExbD-His_6

To increase resolution of ExbB-ExbD-His_6, and complete information gaps attributed to negative-staining EM, cryo-EM of was pursued (Fig. 14B). Optimization of cryo-EM grids was determined at 25 seconds blotting time through the assistance of the FEI Vitrobot Mark IV. The use of low-dose techniques reduced the electron beam to 20 $e^-/Å^2$ at one second exposure time when analyzing the sample on the FEI Tecnai G^2 F20. Data acquisition is currently ongoing, with 1,514 particles collected, and the preliminary 2D projections by the SPARX software suite confirmed observations by negative-staining EM.

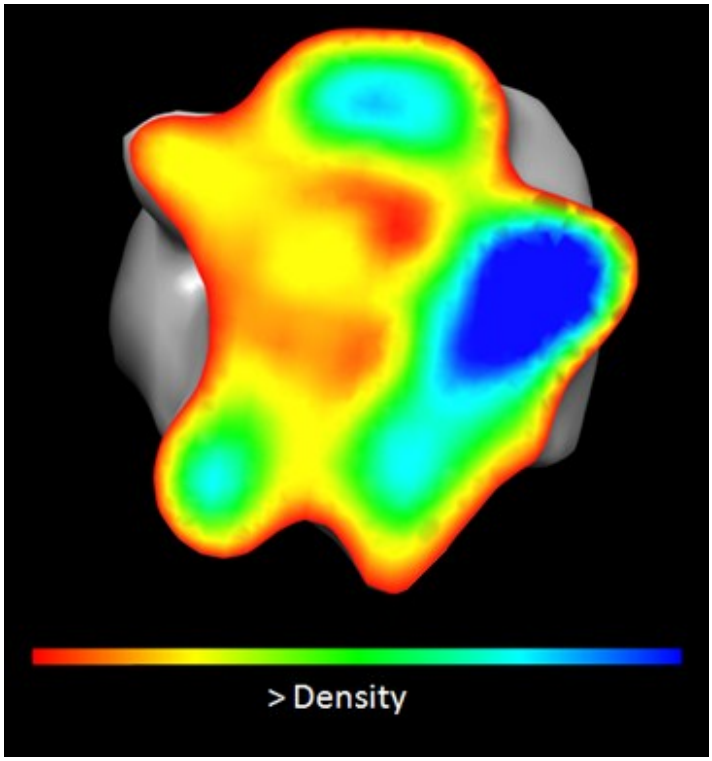

Figure 17. Cross section of the 3DEM density map of ExbB-ExbD. Single particle reconstruction was obtained from 45,321 particles and refined using the SPARX software suite. Cross section is perpendicular to the x-axis. Noticeable in the right region is an area of high density (blue) extending from the complex. ExbD is located predominantly in the periplasm, and due to its flexibility may extend from the complex as observed. Proposed stoichiometry of ExbB and ExbD in the complex is 5:1-2 respectively.

3.7 His_6-ExbB by negative-staining electron microscopy

To confirm observations by EM of ExbB-ExbD-His_6, a construct containing only ExbB with a His_6-tag at the N-terminal end was analyzed by negative-staining EM. Conditions for overexpression of His_6-ExbB were as previously described for the ExbB-ExbD-His_6 complex in Section 2.3. Purification was performed with a 1 mL Profinity IMAC column as previously described in Section 2.4. Following purification by Profinity IMAC, elution fractions were assessed for quality and purity by SDS-PAGE and α-His_6 Western blot. Purification resulted in two prominent bands as observed by silver staining (Fig. 18). The first band, at approximately 26 kDa, denotes full-length ExbB. The second band, at approximately 8 kDa, was proposed to be proteolytic degradation of ExbB based on our previous observations of the ExbB-ExbD-His_6 complex by mass spectrometry. α-His_6 Western blot of the His_6-ExbB purified sample revealed a single band at approximately 26 kDa (Fig. 18). Results suggested that the 8 kDa proteolytic degradation product was formed following purification of His_6-ExbB. There was no band detected on the α-His_6 Western blot at 8 kDa which proposed that the N-terminal end of ExbB was cleaved.

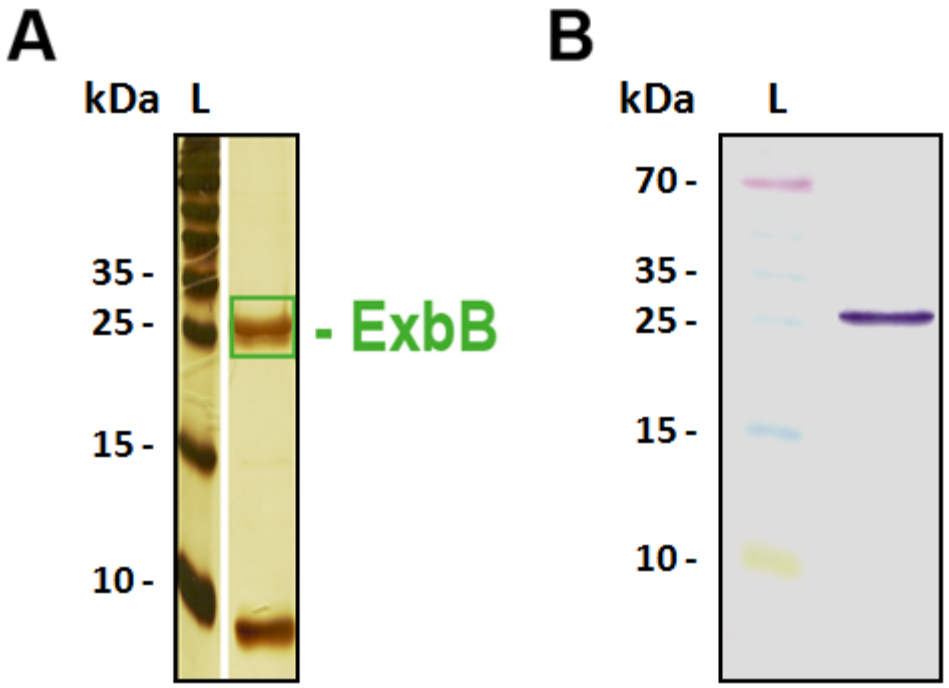

Figure 18. Quality of purified His_6-ExbB. Elution fractions containing His_6-ExbB purified by Profinity IMAC were analyzed by SDS-PAGE and silver stained (A) to evaluate content and purity of the samples. Two prominent bands were observed: 26 kDa represents ExbB and proposed proteolytic degradation of ExbB at 8 kDa. Only full-length ExbB with the His_6-tag appended to the N-terminal end was observed by α-His_6 Western blot (B). L: MW ladder.

Further purification of His_6-ExbB by SEC demonstrated several peaks, the largest of which was predominantly symmetrical at a MW of approximately 270 kDa, suggesting a multi-subunit complex (Fig. 19). The remaining tail-end peaks measured to approximately 8 kDa, suggesting that some of the proteolytic degradation may not be a part of the ExbB complex.

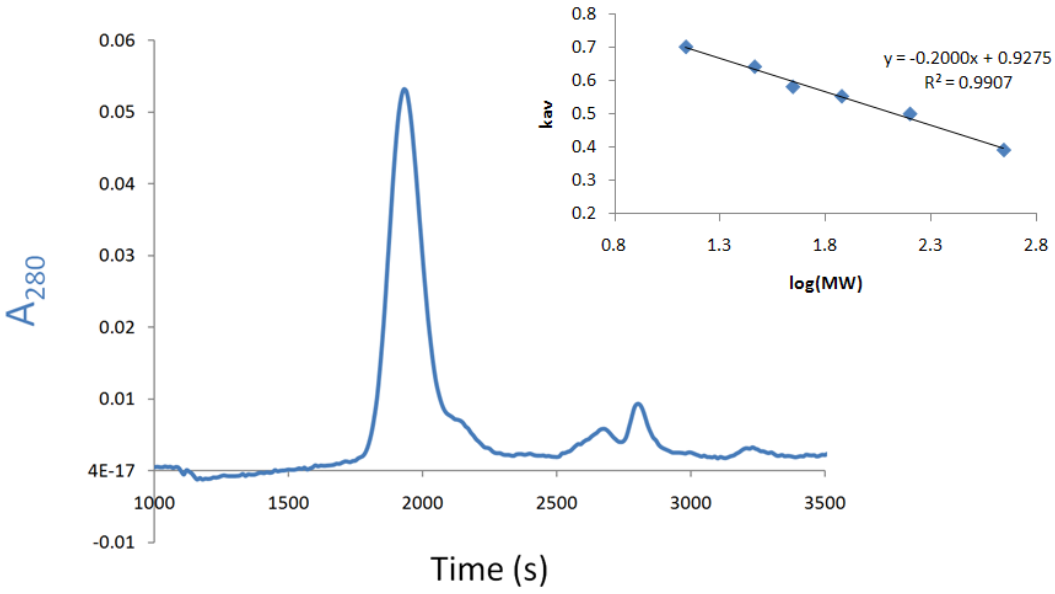

Figure 19. Chromatogram demonstrating the His_6-ExbB complex by SEC. A large symmetrical peak was observed for ExbB. Two smaller peaks observed at 2650 and 2800 seconds elution time were measured to 6 and 8 kDa. The MW of the complex, estimated at 270 kDa, was determined by using the calibration curve prepared for the Superose 6 column from known soluble proteins (upper-right panel).

Following purification by Profinity IMAC, the His_6-ExbB sample was dialysed overnight to remove imidazole as described in Section 2.6. Purified sample was then placed onto glow-discharged carbon-coated EM grids for analysis by negative-staining EM (Fig. 20). Observed were chain-linked particles among few separated particles that showed an approximated diameter of 9 nm. From 320 micrographs collected, 10,296 particles were individually boxed from particles that were not in chain-links using SIGNATURE as previously described in Section 2.10.

To collect separated particles at a faster rate, a second preparation of purified His_6-ExbB was generated (Fig. 20B). The purification protocol was modified by an increased concentration of NaCl, from 100 mM to 200 mM, when eluting His_6-ExbB from the Profinity IMAC column. Results by SDS-PAGE, Western blot and SEC were consistent between both preparations of His_6-ExbB. Increasing the NaCl concentration resulted in the separation of His_6-ExbB particles when observed by negative-staining EM (Fig. 20B).

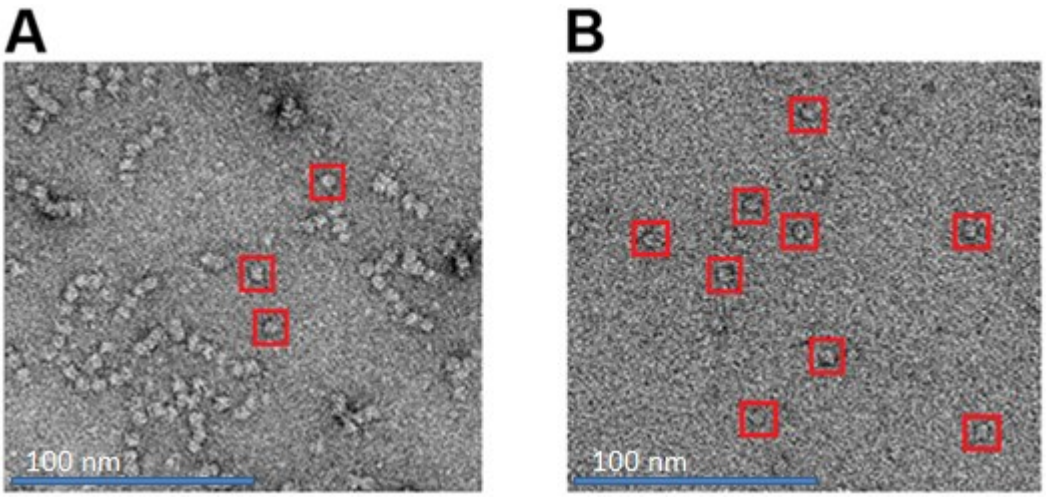

Figure 20. Negative-staining EM of His_6-ExbB. Post-IMAC His_6-ExbB samples were deposited onto glow-discharged carbon-coated EM grids. The grids were stained with uranyl acetate and then observed with a FEI Tecnai G^2 F20 electron microscope. Purified sample #1 showed predominantly chain-linked particles (A). A total of 10,296 particles not in chain-links, as illustrated in red squares, were collected from 320 micrographs. Purified sample #2, following a 100 mM increase in NaCl concentration during elution, exhibited no chain-linked particles (B). A total of 55,872 particles from 560 micrographs of sample #2 were collected for data analysis. For illustration purposes, images were taken at 160,000x magnification. Micrographs for data analysis were collected at 50,000x magnification and adjusted for CTF correction.

From 560 micrographs, a total of 55,872 particles of His_6-ExbB were collected and analyzed. Four class averages, containing 18,238 particles, were generated and further analyzed (Fig. 21).

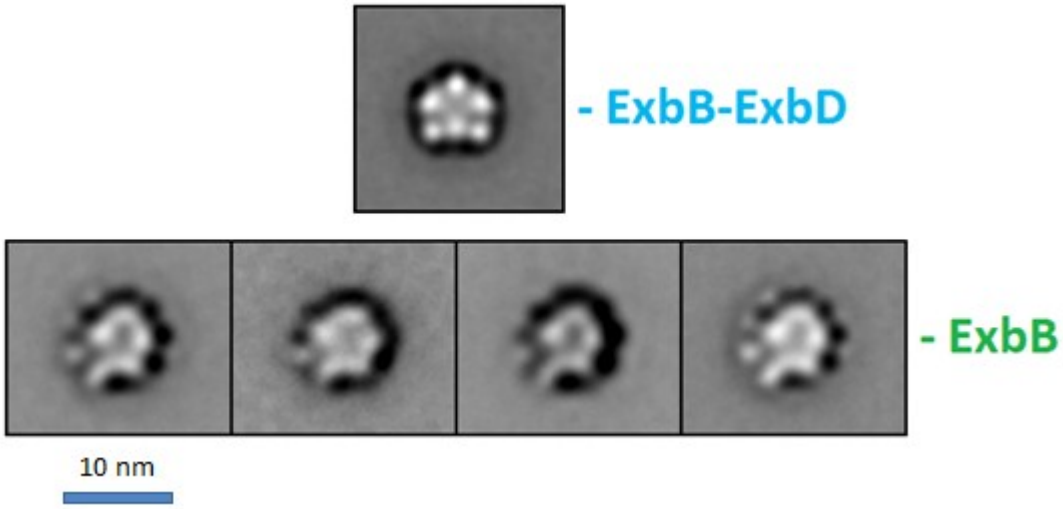

Figure 21. 2D projections of His_6-ExbB by negative-staining EM. From 55,872 particles picked, 18,238 particles analyzed. From individually boxed particles using SIGNATURE, 2D projections were generated using the ML multi-reference alignment method with a total of 12 class averages, four of which are shown. Each class contained approximately 2,800 particles. Refinement of 2D projections by the SPARX software suite did not impose symmetry. An extended clasp was noticeable in the bottom left portions of the 2D projections of His_6-ExbB in comparison to the ExbB-ExbD complex. Unknown by 2D projections was whether this was a possible location of ExbD in the ExbB-ExbD complex, or the extension of the 8 kDa proteolytic degradation attached to the ExbB complex.

Similar to the ExbB-ExbD complex, 300 class averages were generated following several computational rounds of the SPARX software suite from these four classes to generate a 3DEM map. Comparison of cross-sections of the 3DEM density maps of ExbB-ExbD-His_6 and His_6-ExbB were analyzed (Fig. 22). While 3DEM density map showed some degree of error in the lower left lobe for His_6-ExbB, results established ExbB as the dominant protein, supporting observations of five ExbB subunits in the ExbB-ExbD complex (Fig. 22A and B). Comparison of the potential location of ExbD in the ExbB-ExbD complex was compared to ExbB alone (Fig. 22C and D). The observed extension of density protruding out of the center of ExbB-ExbD-His_6 was not present in His_6-ExbB, which suggested that this was a possible location of ExbD in the ExbB-ExbD complex. Given that ExbD is a transmembrane protein, the absence of ExbD in His_6-ExbB may have caused the complex to contract, thus resulting in a smaller diameter of 9 nm as opposed to 10 nm for the ExbB-ExbD complex. When docking ExbB alone into the ExbB-ExbD complex using UCFS Chimera, the extension observed by the red arrow in Figure 22D is the only extension of volume protruding out of ExbB-ExbD-His_6. This suggested that this was either caused by the absence ExbD, or the potential location of the proteolytic degradation that retained onto His_6-ExbB.

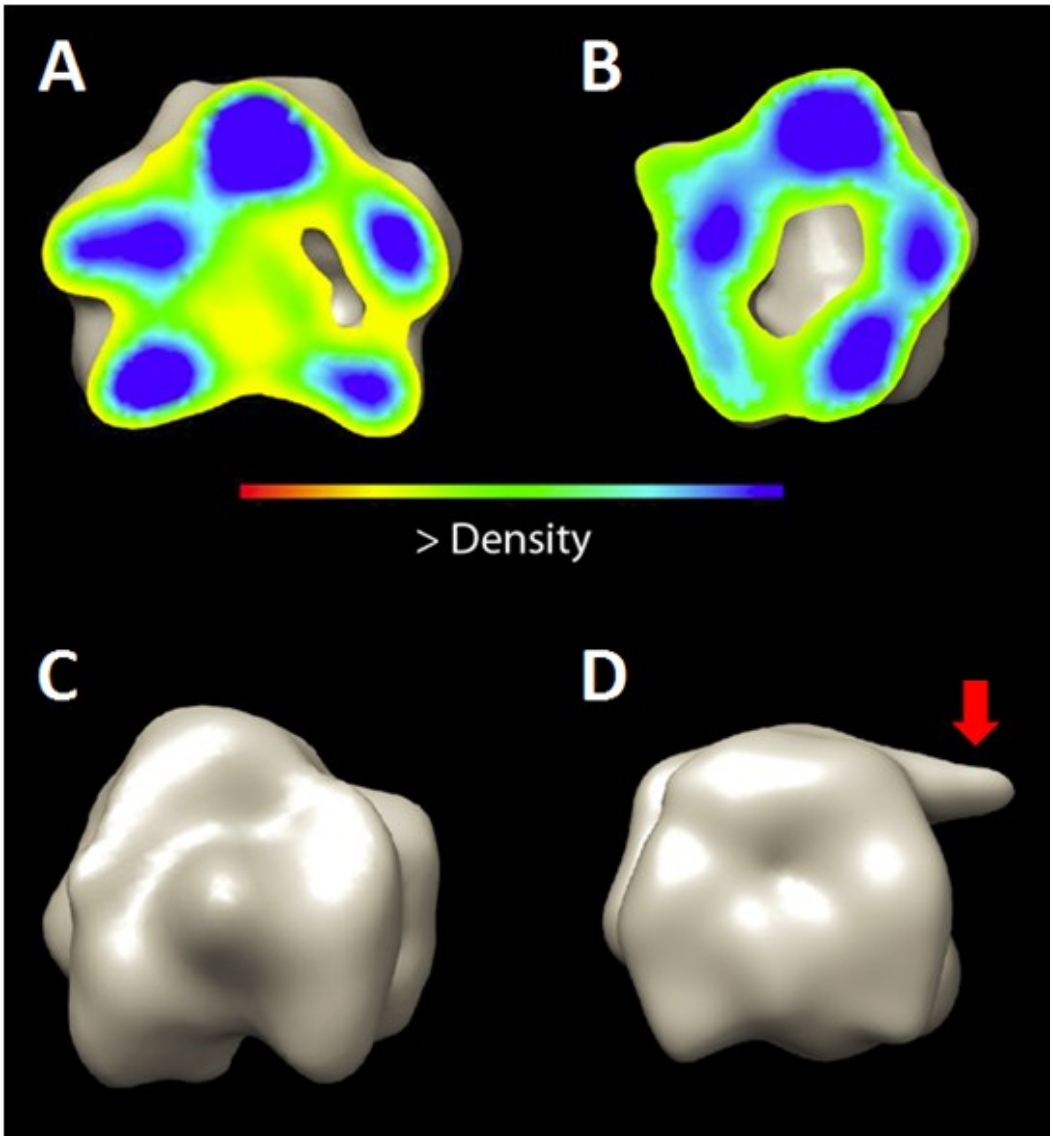

Figure 22. Cross section of the 3DEM map of ExbB-ExbD-His_6 and His_6-ExbB. 3DEM density maps of ExbB-ExbD-His_6 and His_6-ExbB by negative-staining EM. Orientation of the cross section is perpendicular to the x-axis. High density (blue) denotes areas of tightly packed ExbB subunits as measured in 3D space. ExbB in ExbB-ExbD-His_6 demonstrated pentameric organization (A). ExbB also appeared pentameric with a reduction in diameter to 9 nm for His_6-ExbB (B). Mass protruding from the center of the ExbB-ExbD complex denotes possible location of ExbD (C). For ExbB alone, no mass was observed where ExbD is proposed to be located (D). The extension observed in the top right corner of His_6-ExbB (red arrow) is a proposed location of the proteolytic degradation of ExbB as determined by docking by UCFS Chimera.

As the extended mass in His_6-ExbB may be attributed to the proteolytic degradation, a more homogeneous sample purified from SEC was analyzed by negative-staining EM. A total of 6,159 particles were collected and 2D class averages were generated using the SPARX software suite. The 2D projections appeared identical to the data obtained from post-IMAC samples; an extension of mass in the lower left corner was observed similar to Figure 21. Therefore additional particles were not collected to obtain a 3DEM density map.

One result with His_6-ExbB that was not observed with ExbB-ExbD-His_6 was an inconsistency in particles collected. Particles used to generate the 3DEM density map of His_6-ExbB were approximately 30% of total particles collected. Not included in the 3DEM density map observed in Figure 22D were 37,634 particles which were larger sized His_6-ExbB complexes at approximately 14 nm. A total of 23,750 particles were analyzed and a 3DEM density map was generated using the SPARX software suite (Fig. 23A). There was a notable difference in organization for the larger ExbB particles; based on previous observation of chain-linked particles, these were now proposed to be that of the larger His_6-ExbB complexes. Allocation of density in the cross-section suggests three sets of two ExbB monomers are in close proximity to potentially generate trimeric organization (Fig. 23B). Currently, there is no plausible explanation for why His_6-ExbB particles demonstrated two forms of complexes: one that is 9 nm in diameter with a pentameric organization, and the other 14 nm in diameter in a potential trimeric organization.

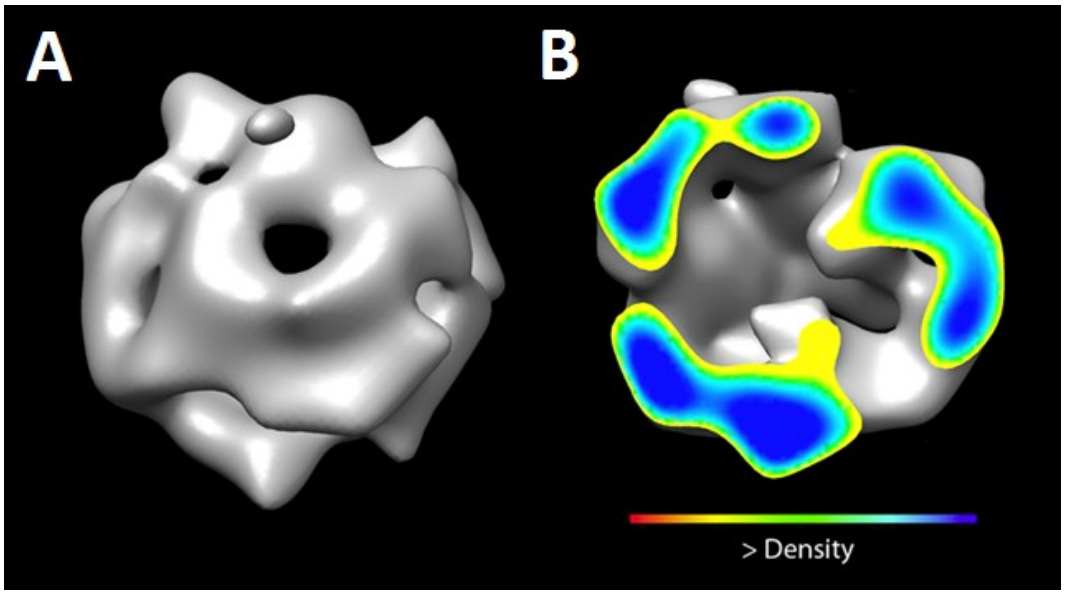

Figure 23. 3DEM density map of larger His_6-ExbB by negative-staining EM. Cross section of the 3DEM map of larger His_6-ExbB. The 3DEM density map was calculated using the SPARX software suite from 23,750 particles. Larger His_6-ExbB particles observed 14 nm in diameter. Holes in the 3DEM density map could suggest missing information or loose binding of the structure. Orientation of the cross section is perpendicular to the x-axis (B). High density (blue) denotes areas of tightly packed ExbB subunits as measured in 3D space. Allocation of density suggests that three sets of two His_6-ExbB monomers in close proximity form trimeric organization.

3.8 GST-TonB-ExbB-ExbD-His_6 constructs

To analyze TonB-ExbB-ExbD in complex by EM, four constructs were generated from pExbBD containing varying lengths of N-terminally tagged GST-TonB. The first plasmid, pALC01, contained amino acids 1-40 which included the transmembrane region of TonB. This construct, GST-*tonB* 1-40 a.a.-*exbB*-exbD-His_6, with all three genes under the control of the T5 promoter, was cloned and tested for expression as described in Section 2.3. Upon analysis of the sequence it was noted that there was no ribosomal binding site prior to *tonB*, resulting in no expression of the three proteins. The second construct, pALC02, was identical to pALC01 with the addition of a ribosomal binding site upstream of gene sequences encoding GST-*tonB* 1-40 a.a. Expression was confirmed by SDS-PAGE and α-GST and α-His_6 Western blots (data not shown).

The third construct, pALC03, terminates TonB immediately before the proline-rich region from residues 66-102. This region was avoided due to its high flexibility and intrinsic degradation of TonB [51]. The *tonB* 1-66 a.a.-*exbB*-*exbD*-His_6 construct covers the cytoplasmic portion of TonB, as well as the transmembrane region and a small portion of the periplasmic region. The fourth construct, pALC04, contained full-length TonB and was designated as GST-*tonB*-*exbB*-*exbD*-His_6. Expression of this construct was confirmed by following protocol as described in Section 2.3. Purification was performed with a Glutathione-Sepharose column to capture the complex by GST-tagged TonB. Purification of

GST-TonB-ExbB-ExbD-His_6 by Glutathione-Sepharose column resulted in a single band denoting GST-TonB at approximately 55 kDa by α-GST Western blot (Fig. 24A). His_6-tagged ExbD resulted in a band at approximately 16 kDa by α-His_6 Western blot (Fig. 24B). Results suggest that GST-tagged TonB and His_6-tagged ExbD co-purified, and given ExbD`s interactions with ExbB as previously described, the three proteins are proposed to have purified in complex.

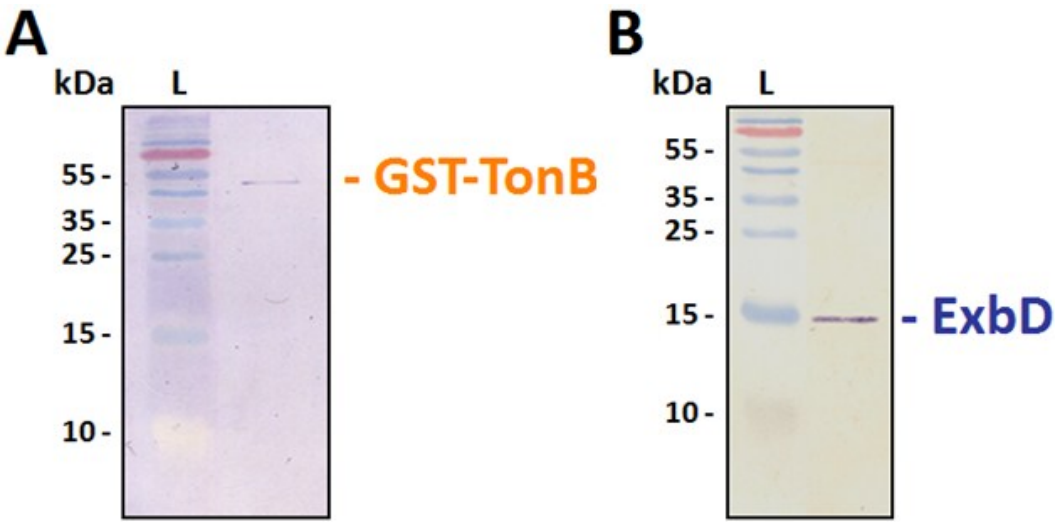

Figure 24. Detection of full-length GST-TonB-ExbB-ExbD-His_6 by Western blot analysis. Solubilized total membranes in DDM containing GST-TonB-ExbB-ExbD-His_6 were applied to a 5 ml Glutathione-Sepharose column to capture the complex by GST-tagged TonB. Elution fractions were analysed by Western blots to evaluate content of the samples. (A) α-GST detected GST-tagged TonB, and α-His_6 (B) detected His_6-tagged ExbD. L: MW ladder.

Chapter 4: Discussion and Conclusion

4.1 Discussion

Interaction between ExbB and ExbD proteins within a complex to harness the PMF to energize the OM has been well documented [64]. However, mechanisms of their function remain elusive since much of ExbB and ExbD are structurally unknown. While a high-resolution structure of the C-terminal periplasmic domain of ExbD has been solved by NMR, structural information is lacking for the membrane-spanning regions of both ExbB and ExbD. The stoichiometry, native organization of ExbB and ExbD in complex, and the molecular mechanism of proton translocation remain undetermined. Determining the structural organization of the ExbB-ExbD complex will provide insight into energy-dependent nutrient import in bacteria.

A high-quality preparation of purified protein is necessary to analyze by EM. As many proteins in nature do not have an affinity toward metal ions, the use of a His_6-tag facilitates the purification of proteins. Based on observations of interactions between ExbB and TonB, ExbB has been proposed to act as a scaffold protein and may act to stabilize ExbD [64]. To purify ExbB and ExbD in complex, the His_6-tag was appended to the C-terminal end of ExbD which had been previously solved by NMR. ExbB-ExbD-His_6 was successfully purified in complex as confirmed by SDS-PAGE stained by Coomassie and silver. Consistent purifications of ExbB-ExbD-His_6 demonstrated their interaction *in vitro*. Analysis

by SDS-PAGE involves denaturing conditions to visualize individual proteins, but does not determine whether ExbB-ExbD-His_6 is a stable complex. Therefore, to further analyze the stability and homogeneity of ExbB-ExbD-His_6 purification by SEC was performed.

Determination of protein structures requires non-aggregated, homogenous purified sample preparations. Purification by SEC demonstrated a single symmetrical peak for ExbB-ExbD-His_6, confirming ExbB co-purified with ExbD by Profinity IMAC. Estimated MW of 350 kDa for ExbB-ExbD-His_6 suggested a multi-subunit complex in the presence of DDM detergent. Previous studies on membrane proteins suggested DDM artificially increased by up to double the MW [100]. Furthermore, SEC separates proteins on their frictional coefficient in relation to known soluble proteins in a standard curve. Therefore, the predicted MW for ExbB-ExbD-His_6 would be expected to be approximately 200 kDa.

Consistent purified preparations of ExbB-ExbD-His_6 were amenable for further study by EM. Purified preparations were negatively stained with uranyl acetate to preserve the sample onto the EM grid. Uranyl acetate is a simple stain that sufficiently enhances the phase contrast by exposing the sample to solutions containing a higher atomic weight. The electron beam in the TEM is less deflected as it passes through the sample, as opposed to passing through the stain. Electrons that are highly deflected are removed by the objective aperture in the TEM located below the EM grid. The phase contrast of the image is

dependent on how many electrons are deflected. However, there are limitations of using heavy ions to increase the contrast, as the use of uranyl acetate may distort ExbB-ExbD-His_6. Furthermore, particles of interest may demonstrate a preferred orientation when falling onto the EM grid prior to being stabilized by uranyl acetate. Nonetheless, the simple nature of uranyl acetate provides the best option for preliminary analysis of protein complexes by negative-staining.

Micrographs collected by the FEI Tecnai T12 electron microscope demonstrated uniform particles, approximately 10 nm in diameter. The increased electron beam damage caused by the absence of low-dose conditions on the FEI Tecnai T12, prevented data acquisition of particles. Observations by negative-staining EM demonstrated particles were amenable to single-particle reconstruction by collecting high-quality images on the FEI Tecnai G^2 F20.

A total of 45,321 particles of ExbB-ExbD-His_6 complex were collected. The number of particles collected for 2D reconstruction is a key determinant in achieving significant resolution. Particles were collected using the software SIGNATURE. Recent advancements in particle picking programs have had success in avoiding manually picking of particles, a highly difficult process that is time consuming, and subject to noise and low contrast in addition to human interpretations of data. The 2D template was derived from manually picking particles without reference bias. Four out of six classes were the best representations of the possible structure and selected as a reference template.

Once the template was selected, the cross-correlation function between the micrograph and the 2D reference template was calculated using Fourier methods [92]. Peaks obtained from the cross-correlation function map provided the probable locations of particles in the micrograph. The maximum height of the peak could be set so that there was sufficient differentiation between particles of interest and background noise. When particles of ExbB-ExbD-His_6 were selected in SIGNATURE, each particle was analyzed individually and particles that were not uniform to the overall average, approximately 5% of particles, were deleted.

Once particles were individually boxed, the SPARX software suite was used to separate particles into respective classes based on their position onto the EM grid. The SPARX software suite contains the new generation of 2D and 3D alignment tools for processing data based on the ML approach to multi-refinement alignment. The standard for EM processing is the EMAN 2 software, and the SPARX software suite uses this as its initial library [93]. Given the SPARX software suite has many novel features, generating class averages requires a less stringent data sampling. Initial observations of the 2D projections suggested a pentameric organization for the ExbB-ExbD complex. Five dominant areas of density, highlighted as white lobes, suggested that these were potentially cylindrical structures. Unknown was whether the areas of density that demonstrated pentameric organization was ExbB or ExbD, or a mixture of the two proteins.

To gain perspective on the overall dimensions of ExbB-ExbD-His_6, a 3DEM density map was pursued. Through the SPARX software suite, a 3DEM density map of 22.5 Å resolution was generated. In examining the results obtained for the 3DEM density map, five vertical volumes extending across the complex confirmed observations by 2D averaging. These measured at approximately 8 nm in height, proposing that each one is a single transmembrane protein, comparable to the height of the CM, measured at 7.5 nm [101]. Given that ExbB is considered the scaffolding protein in the complex, and *in vivo* studies propose a stoichiometry of 7:2 for ExbB:ExbD, ExbB was suggested as the protein in pentameric organization, while ExbD is proposed to extend out of the complex.

To obtain a greater resolution and gain more information covered by negative-staining, cryo-EM of ExbB-ExbD-His_6 was pursued. Initial findings demonstrated particles similar to those observed by negative-staining EM. Preliminary 2D averages of ExbB-ExbD-His_6 by cryo-EM confirmed observations by negative-staining; however more particles are required to obtain a 3DEM density map.

The stoichiometry of ExbB in ExbB-ExbD-His_6 corresponds to a previously reported study [102]. Pramanik *et al*. analyzed miniscule amounts of protein and determined by small-angle X-ray scattering (SAXS) that a complex of ExbB in DM (ExbB-DM) contained approximately 4.88 monomers [102]. This result was comparable to that of ExbB-ExbD-His_6, as a miniscule amount of protein was

analyzed to determine pentameric organization of the complex by negative-staining EM.

In an attempt to elucidate which of the two proteins potentially demonstrated pentameric organization, His_6-ExbB was generated with the His_6-tag appended to the N-terminal end of ExbB. Purification of His_6-ExbB by Profinity IMAC was confirmed by SDS-PAGE that was silver stained and by Western blot analysis. Proteolytic degradation of ExbB was proposed to occur following purification given previous work on ExbB-ExbD-His_6 by mass spectrometry.

Purification of His_6-ExbB by SEC demonstrated one major symmetrical peak of His_6-ExbB at approximately 270 kDa, followed by two small degradation peaks. Pramanik *et al.* reported similar SEC observations with ExbB-DM, demonstrating a major symmetrical peak, followed by two small degradation peaks [102]. Also corresponding with SEC findings for His_6-ExbB in DDM, the MW of the large peak for ExbB-DM was estimated between 290 and 310 kDa. A difference of 20 kDa between His_6-ExbB in DDM and ExbB-DM could be attributed to the specificity of the column, the standards used to estimate the MWs, and the effect of using different detergents for purification.

Initial findings of His_6-ExbB by negative-staining EM highlighted many particles clasped together in chain-linked formation. Considering that both ExbB and ExbD proteins function together to harness the PMF, ExbB alone may have

disrupted stability of the complex, resulting in particles of His_6-ExbB to attach through hydrophobic interactions.

A second purification of His_6-ExbB by Profinity IMAC was performed to physically separate particles by increasing NaCl concentration during elution. The purified sample of His_6-ExbB with increased NaCl concentration was analyzed by negative-staining EM and resulted in separated particles. His_6-ExbB particles 9 nm in diameter were collected and 2D projections were generated. While a pentameric organization was potentially observed, there was also an extension of mass approximately 2.5 nm in length and 1 nm in height, suggesting the possible location of the proteolytic degradation.

A 3DEM density map was obtained at a resolution of approximately 25 Å and observations confirmed ExbB as the protein that demonstrated pentameric organization in the ExbB-ExbD-His_6 complex. This was determined by analyzing similar positions of increased density in cross-sections of 3DEM density maps of ExbB-ExbD-His_6 and His_6-ExbB complexes. In comparison to the 3DEM density map of the ExbB-ExbD-His_6 complex, the His_6-ExbB complex experiences a contraction of the overall structure with a reduced diameter from approximately 10 nm to 9 nm. This was also observed as the ExbBs in the His_6-ExbB complex appeared more compact with respect to the distance of one another. This may be due to the absence of ExbD in the His_6-ExbB complex, which could also affect proton channel formation. As such, when ExbD is present in the ExbB-ExbD-His_6

complex, the diameter was increased given the greater separation of the ExbB proteins; this may potentially allow for the proton channel to form near the center of the complex. The significance of maintaining the structural integrity of the protein complex, as observed when ExbD was absent in the larger His_6-ExbB complex, potentially demonstrates that both ExbB and ExbD are required for proton channel formation.

When comparing the possible location of ExbD in 3DEM density maps, the area of greatest density extending from the ExbB-ExbD-His_6 complex was not observed for His_6-ExbB. This suggested the periplasmic region of ExbD extends out of the complex and may provide the orientation of the complex. At low resolution, it was not possible to determine whether one or two ExbD proteins existed in the complex. As previously described, the conserved TM domains of TolR and MotB are each essential for their own activity. Specifically, residues involved in homodimerization are integral to these proton channels. Given ExbD shares sequence homology with TolR and MotB, there is precedent for the potential homodimerization of ExbD in the ExbB-ExbD-His_6 complex. Given the high density where ExbD is proposed to be located is contained in a small area as observed in the 3DEM density map of ExbB-ExbD-His_6, a visual representation of whether ExbD homodimerizes may only be determined once a crystal structure is obtained.

A second 3DEM density map was generated for the His_6-ExbB complex from 37,634 larger sized particles at approximately 14 nm in diameter. As the larger particles were not observed for the ExbB-ExbD-His_6 complex by negative-staining EM, their formation was potentially caused from the absence of ExbD in the His_6-ExbB complex. More specifically, the structural integrity of the complex may have been compromised at the location of ExbD, given its high area of density as observed in the 3DEM density map of ExbB-ExbD-His_6. As a result, small His_6-ExbB complexes which lacked this area due to the absence of ExbD may have bound to each other through hydrophobic interactions to generate complexes potentially containing 12 ExbB monomers in trimeric organization. However, the 3DEM density map of the larger His_6-ExbB complex contained significant missing information as observed by the many absences of density throughout the complex. Given these larger particles were not observed in the ExbB-ExbD-His_6 complex and as the proposed role of ExbB and ExbD as an energetic source in nature requires both proteins in complex, the result of the overall structure of the larger His_6-ExbB complex was not predicted to exist in nature.

Structural information obtained by EM provides the first visualization of ExbB-ExbD-His_6 to further our understanding of the mechanism of energy-dependent nutrient import in bacteria. Considering the stoichiometry of ExbB-ExbD-His_6 and His_6-ExbB obtained by EM suggests a ratio of 5:1-2 for ExbB:ExbD, it is unclear whether calculations of protein concentration accurately reflect the

in vivo stoichiometry of 7:2 [68]. Cell numbers used to calculate the abundance of these proteins *in* vivo is based on estimation, given that non-synchronous growth of cells resulted in varied sizes with possible differences in active TonB-ExbB-ExbD. Viability assays may underestimate the total number of cells present, further confounding the estimated stoichiometry. As such, a stoichiometry of 5:1-2 for ExbB:ExbD is potential *in vivo*, although the stoichiometry remains unknown when in complex with TonB *in vitro*. Understanding the stoichiometry and organization of ExbB and ExbD in complex gives insight into energy transduction between membranes in the cell envelope of Gram-negative bacteria.

4.2 Future Directions

Currently the orientation of the 3DEM density maps of ExbB-ExbD-His_6, and His_6-ExbB, in relation to the cytoplasmic and periplasmic regions have yet to be determined. Considering ExbD is predominantly located in the periplasm, the extension of density that is predicted to be ExbD in the 3DEM density map of ExbB-ExbD-His_6 is directed towards the periplasm. To elucidate further, the use of α-His_6 antibodies bound to His_6-tagged ExbD and EM analysis could be applied. However, an antibody would be physically too large and potentially obstruct any pertinent information of the complex. Therefore, once confirmation that the ExbB-ExbD-His_6 particles bind to the antibody is obtained, use of a fragment antigen-binding (Fab) portion to determine the orientation of ExbD in ExbB-

ExbD-His_6 is a viable option. A Fab fragment designed to bind to the His_6-tag of ExbD would be possible considering its availability during purification by Profinity IMAC. Due to its MW, the Fab fragment would be too small to be seen bound to individual particles, but will be observed as an extension of mass in 2D projections.

A similar strategy is currently in progress to determine the orientation of the complex through the application of pre-labelled 5 nm Ni-NTA nanogold particles as a mixture into the purified preparation. Ni-NTA nanogold particles would bind to the His_6-tag appended to the C-terminal end of ExbD and the interaction would be observed by 2D projections. One advantage of using 5 nm Ni-NTA nanogold particles as opposed to the standard 2 nm Ni-NTA nanogold particles is that no specialized staining is required for resolution of gold labels. However, given that particles of ExbB-ExbD-His_6 are approximately 10 nm in diameter, the smaller 2 nm Ni-NTA nanogold particles may also be explored if the larger 5 nm Ni-NTA nanogold particles hide pertinent information of the particles. Due to the heavy contrast of 2 nm Ni-NTA nanogold particles, using uranyl acetate as a negative stain would coat pertinent information and the location of binding would not be observed. To alleviate this, the use of NanoVan as a negative-staining reagent could be applied [103]. NanoVan is based on vanadium, a lower atomic stain than uranium, and is predominantly used to detect samples labelled with 2 nm Ni-NTA nanogold particles.

The use of cryo-EM for single particle analysis is in progress. Complementing these studies are crystallization trials that are currently underway in the Coulton Laboratory. Particles of ExbB-ExbD-His_6 are being collected to obtain a sub-10 Å resolution 3DEM density map for comparison to a future crystal structure. The use of cryo-EM on His_6-ExbB will be a future focus. Once 2D crystals are obtained, they could be analyzed by EM through a strategy known as freeze-fracturing [104]. This strategy requires cryogenic conditions where the frozen 2D crystals are then fractured to expose the proteins on an open surface. Placing a platinum carbon replica of the exposed proteins and removing the organic compounds underneath would be required for data collection.

Data acquisition would be complex as the irregular carbon film would cause diffraction at all angles of the 2D crystal. To circumvent this, cross-correlation methods could be used to determine the translational disorder in 2D crystals to generate an overall organization. This could potentially yield an even higher resolution than single particle analysis by cryo-EM. Studying 2D crystals requires extended time to produce crystals and to analyze by EM. However, once achieved, the ExbB-ExbD-His_6 2D crystal structure could be confirmed by docking into the 3DEM density map. Since a crystal structure would only show one conformation of the ExbB-ExbD-His_6, combining both techniques could provide visualization of other possible conformations of ExbB-ExbD-His_6.

Current studies in Coulton Laboratory are focusing on the structural determination of the TonB-ExbB-ExbD complex. To elucidate interactions that occur at the inner membrane between TonB, ExbB and ExbD, three constructs of TonB were cloned into pExbBD, resulting in pALC02, pALC03 and pALC04. The genes encoding pALC02 were selected as it contained the minimal sequence of TonB that still encompasses its transmembrane domain, along with a few additional amino acids in the periplasm to stabilize its integration. The second plasmid, pALC03, terminates TonB immediately before its proline-rich region from residues 66-102. This region was avoided as it is highly flexible and is a proposed site for intrinsic degradation of TonB [51]. In addition to decreasing the amount of degradation of TonB, these two truncated TonB constructs provide future mapping of specific regions of interaction between the transmembrane regions of TonB-ExbB-ExbD by comparing their binding properties to those of full-length TonB. Optimization in the yield of pALC04 would provide sufficient material for crystallization trials and the generation of a 3DEM density map by EM to further our understanding on the mechanism of nutrient import in bacteria.

4.3 Summary

To investigate properties of ExbB-ExbD-His_6 from *E. coli*, *exbB* and *exbD* genes were cloned and optimized recombinant protein expression. After solubilization of total membranes in DDM, ExbB co-purified with His-tagged ExbD

by Profinity IMAC, demonstrating ExbD-ExbB interaction *in vitro*. SEC identified a PDC with a MW of approximately 350 kDa. Recombinant His_6-tagged ExbB was also expressed and purified; this PDC corresponded to a MW of 270 kDa by SEC.

To elucidate the structural conformation of ExbB and ExbD, the protein complex was analyzed by negative-staining EM. Observations by low-dose negative-staining EM revealed uniform particles approximately 10 nm in diameter for ExbB-ExbD-His_6; initial observations by cryo-EM supported these findings.

By single-particle analysis from high-resolution negative-staining EM images, 2D projections were generated using the SPARX software suite. Using the FEI Tecnai G^2 F20, a total of 45,321 particles for ExbB-ExbD-His_6 were collected from 131 micrographs. These particles were then individually separated and boxed using SIGNATURE. Boxed particles were distributed into 12 different orientation classes based on the ML approach to multi-refinement alignment. After several rounds, particles in each respective class were averaged, and projections were refined using the SPARX software suite.

Analysis of the 2D projections suggested a symmetrical pentameric organization for ExbB-ExbD-His_6. To confirm these results, 55,872 particles of His_6-tagged ExbB were collected and 18,238 particles analyzed. Particles were observed at approximately 9 nm in diameter, and 2D projections confirmed pentameric organization. This result established ExbB as the dominant protein,

providing five ExbB subunits in ExbB-ExbD-His_6. The 2D projections allowed the generation of a 3D reconstruction. Several rounds of computational operations using the SPARX software suite created a 3DEM density map of the ExbB-ExbD complex, resolved to a resolution of 22.5 Å.

Analysis of the 22.5 Å 3DEM map confirmed a pentameric organization of ExbB in ExbB-ExbD-His_6, with each ExbB subunit having a height of approximately 8 nm. Since ExbB is a transmembrane protein, this dimension is sufficient to span the CM with its reported thickness of approximately 7.5 nm [101]. A difference in quality of one of the five ExbB subunits shown is common in negative-staining EM due to particles having favourable binding to carbon-coated EM grids. Loss of information is less prevalent in cryo-EM due to the sample being contained in vitreous ice. Based on its extended periplasmic region, ExbD was proposed to be located in an extension of density in the upper region of the 3DEM map. Currently unknown is whether there is a monomer or dimer of ExbD within the complex. If there was a dimer of ExbD, volume thickness in the 3DEM density map projects that the two ExbD subunits would be in proximity to potentially interact within the CM complex.

Results obtained for ExbB-ExbD-His_6 by negative-staining EM demonstrates the need to generate a 3DEM density map by cryo-EM. A sub-10 Å resolution structure would provide an understanding on how the organization of the complex is involved in achieving proton translocation across the CM.

Generating a high-resolution 3DEM density map of the GST-TonB-ExbB-ExbD-His_6 complex will provide further insight into the mechanism of energy-dependent nutrient import in bacteria. 3DEM density maps generated will also provide a template onto which the 3D crystal structure may be mapped.

References

1. Murray, P., Rosenthal, K., and Pfaller, M. , *Medical Microbiology*, 6th ed., Mosby Elsevier, Philadelphia, PA. 2009. p. 1-6.
2. Anderson, R.G. and K. Jacobson, *A role for lipid shells in targeting proteins to caveolae, rafts, and other lipid domains.* Science, 2002. **296**(5574): p. 1821-5.
3. Morrison, D.C. and L.F. Kline, *Activation of the classical and properdin pathways of complement by bacterial lipopolysaccharides (LPS).* Journal of immunology, 1977. **118**(1): p. 362-8.
4. Ruiz, N., D. Kahne, and T.J. Silhavy, *Transport of lipopolysaccharide across the cell envelope: the long road of discovery.* Nature reviews. Microbiology, 2009. **7**(9): p. 677-83.
5. Sperandeo, P., et al., *Functional analysis of the protein machinery required for transport of lipopolysaccharide to the outer membrane of Escherichia coli.* Journal of bacteriology, 2008. **190**(13): p. 4460-9.
6. Meroueh, S.O., et al., *Three-dimensional structure of the bacterial cell wall peptidoglycan.* Proceedings of the National Academy of Sciences of the United States of America, 2006. **103**(12): p. 4404-9.
7. Dmitriev, B., F. Toukach, and S. Ehlers, *Towards a comprehensive view of the bacterial cell wall.* Trends in microbiology, 2005. **13**(12): p. 569-74.
8. Demchick, P. and A.L. Koch, *The permeability of the wall fabric of Escherichia coli and Bacillus subtilis.* Journal of bacteriology, 1996. **178**(3): p. 768-73.
9. Fecycz, I.T. and J.N. Campbell, *Mechanisms of activation and secretion of a cell-associated precursor of an exocellular protease of Pseudomonas aeruginosa 34362A.* European journal of biochemistry, 1985. **146**(1): p. 35-42.
10. Silhavy, T.J., D. Kahne, and S. Walker, *The bacterial cell envelope.* Cold Spring Harbor perspectives in biology, 2010. **2**(5): p. a000414.
11. Nikaido, H., *Molecular basis of bacterial outer membrane permeability revisited.* Microbiology and molecular biology reviews, 2003. **67**(4): p. 593-656.
12. Koebnik, R., K.P. Locher, and P. Van Gelder, *Structure and function of bacterial outer membrane proteins: barrels in a nutshell.* Molecular microbiology, 2000. **37**(2): p. 239-53.
13. Schirmer, T., *General and specific porins from bacterial outer membranes.* Journal of structural biology, 1998. **121**(2): p. 101-9.
14. Harder, K.J., H. Nikaido, and M. Matsuhashi, *Mutants of Escherichia coli that are resistant to certain beta-lactam compounds lack the ompF porin.* Antimicrobial agents and chemotherapy, 1981. **20**(4): p. 549-52.
15. Nikaido, H. and M. Vaara, *Molecular basis of bacterial outer membrane permeability.* Microbiological reviews, 1985. **49**(1): p. 1-32.
16. Ulmke, C., et al., *Site-directed mutagenesis of loop L3 of sucrose porin ScrY leads to changes in substrate selectivity.* Journal of bacteriology, 1999. **181**(6): p. 1920-3.
17. Klebba, P.E., *Mechanism of maltodextrin transport through LamB.* Research in microbiology, 2002. **153**(7): p. 417-24.
18. Schauer, K., D.A. Rodionov, and H. de Reuse, *New substrates for TonB-dependent transport: do we only see the 'tip of the iceberg'?* Trends in biochemical sciences, 2008. **33**(7): p. 330-8.

19. Chakraborty, R., E. Storey, and D. van der Helm, *Molecular mechanism of ferricsiderophore passage through the outer membrane receptor proteins of Escherichia coli.* Biometals, 2007. **20**(3-4): p. 263-74.
20. Crosa, J.H. and C.T. Walsh, *Genetics and assembly line enzymology of siderophore biosynthesis in bacteria.* Microbiology and molecular biology reviews, 2002. **66**(2): p. 223-49.
21. Ferguson, A.D., et al., *Siderophore-mediated iron transport: crystal structure of FhuA with bound lipopolysaccharide.* Science, 1998. **282**(5397): p. 2215-20.
22. Ferguson, A.D., et al., *Structural basis of gating by the outer membrane transporter FecA.* Science, 2002. **295**(5560): p. 1715-9.
23. Hantke, K., et al., *Salmochelins, siderophores of Salmonella enterica and uropathogenic Escherichia coli strains, are recognized by the outer membrane receptor IroN.* Proceedings of the National Academy of Sciences of the United States of America, 2003. **100**(7): p. 3677-82.
24. Fairman, J.W., N. Noinaj, and S.K. Buchanan, *The structural biology of beta-barrel membrane proteins: a summary of recent reports.* Current opinion in structural biology, 2011. p. 1-9.
25. Ferguson, A.D. and J. Deisenhofer, *TonB-dependent receptors-structural perspectives.* Biochimica et biophysica acta, 2002. **1565**(2): p. 318-32.
26. Schramm, E., et al., *Nucleotide sequence of the colicin B activity gene cba: consensus pentapeptide among TonB-dependent colicins and receptors.* Journal of bacteriology, 1987. **169**(7): p. 3350-7.
27. Yang, A.S. and B. Honig, *Free energy determinants of secondary structure formation: I. alpha-Helices.* Journal of molecular biology, 1995. **252**(3): p. 351-65.
28. Pawelek, P.D., et al., *Structure of TonB in complex with FhuA, E. coli outer membrane receptor.* Science, 2006. **312**(5778): p. 1399-402.
29. Chimento, D.P., et al., *Substrate-induced transmembrane signaling in the cobalamin transporter BtuB.* Nature structural biology, 2003. **10**(5): p. 394-401.
30. Larsen, R.A., et al., *Identification of TonB homologs in the family Enterobacteriaceae and evidence for conservation of TonB-dependent energy transduction complexes.* Journal of bacteriology, 1996. **178**(5): p. 1363-73.
31. James, K.J., et al., *TonB induces conformational changes in surface-exposed loops of FhuA, outer membrane receptor of Escherichia coli.* Protein science, 2008. **17**(10): p. 1679-88.
32. Krewulak, K.D. and H.J. Vogel, *Structural biology of bacterial iron uptake.* Biochimica et biophysica acta, 2008. **1778**(9): p. 1781-804.
33. Quiocho, F.A. and P.S. Ledvina, *Atomic structure and specificity of bacterial periplasmic receptors for active transport and chemotaxis: variation of common themes.* Molecular microbiology, 1996. **20**(1): p. 17-25.
34. Davidson, A.L., et al., *Structure, function, and evolution of bacterial ATP-binding cassette systems.* Microbiology and molecular biology reviews, 2008. **72**(2): p. 317-64.
35. Pohl, A., P.F. Devaux, and A. Herrmann, *Function of prokaryotic and eukaryotic ABC proteins in lipid transport.* Biochimica et biophysica acta, 2005. **1733**(1): p. 29-52.
36. Borths, E.L., et al., *The structure of Escherichia coli BtuF and binding to its cognate ATP binding cassette transporter.* Proceedings of the National Academy of Sciences of the United States of America, 2002. **99**(26): p. 16642-7.
37. Davidson, A.L. and J. Chen, *ATP-binding cassette transporters in bacteria.* Annual review of biochemistry, 2004. **73**: p. 241-68.

38. Locher, K.P., A.T. Lee, and D.C. Rees, *The E. coli BtuCD structure: a framework for ABC transporter architecture and mechanism.* Science, 2002. **296**(5570): p. 1091-8.
39. Hvorup, R.N., et al., *Asymmetry in the structure of the ABC transporter-binding protein complex BtuCD-BtuF.* Science, 2007. **317**(5843): p. 1387-90.
40. Newstead, S., et al., *Insights into how nucleotide-binding domains power ABC transport.* Structure, 2009. **17**(9): p. 1213-22.
41. Hollenstein, K., R.J. Dawson, and K.P. Locher, *Structure and mechanism of ABC transporter proteins.* Current opinion in structural biology, 2007. **17**(4): p. 412-8.
42. Jormakka, M., B. Byrne, and S. Iwata, *Protonmotive force generation by a redox loop mechanism.* Federation of european biochemical societies, 2003. **545**(1): p. 25-30.
43. Chu, B.C., R.S. Peacock, and H.J. Vogel, *Bioinformatic analysis of the TonB protein family.* Biometals, 2007. **20**(3-4): p. 467-83.
44. Derouiche, R., et al., *Protein complex within Escherichia coli inner membrane. TolA N-terminal domain interacts with TolQ and TolR proteins.* Journal of biological chemistry, 1995. **270**(19): p. 11078-84.
45. Sturgis, J.N., *Organisation and evolution of the tol-pal gene cluster.* Journal of molecular microbiology and biotechnology, 2001. **3**(1): p. 113-22.
46. Cascales, E., et al., *Proton motive force drives the interaction of the inner membrane TolA and outer membrane pal proteins in Escherichia coli.* Molecular microbiology, 2000. **38**(4): p. 904-15.
47. Germon, P., et al., *Energy-dependent conformational change in the TolA protein of Escherichia coli involves its N-terminal domain, TolQ, and TolR.* Journal of bacteriology, 2001. **183**(14): p. 4110-4.
48. Zhou, J., et al., *Function of protonatable residues in the flagellar motor of Escherichia coli: a critical role for Asp 32 of MotB.* Journal of bacteriology, 1998. **180**(10): p. 2729-35.
49. Chang, C., et al., *Crystal structure of the dimeric C-terminal domain of TonB reveals a novel fold.* Journal of biological chemistry, 2001. **276**(29): p. 27535-40.
50. Larsen, R.A., G.E. Wood, and K. Postle, *The conserved proline-rich motif is not essential for energy transduction by Escherichia coli TonB protein.* Molecular microbiology, 1994. **12**(5): p. 857.
51. Khursigara, C.M., et al., *Deletion of the proline-rich region of TonB disrupts formation of a 2:1 complex with FhuA, an outer membrane receptor of Escherichia coli.* Protein science, 2005. **14**(5): p. 1266-73.
52. Koedding, J., et al., *Dimerization of TonB is not essential for its binding to the outer membrane siderophore receptor FhuA of Escherichia coli.* Journal of biological chemistry, 2004. **279**(11): p. 9978-86.
53. Khursigara, C.M., et al., *Enhanced binding of TonB to a ligand-loaded outer membrane receptor: role of the oligomeric state of TonB in formation of a functional FhuA.TonB complex.* The Journal of biological chemistry, 2004. **279**(9): p. 7405-12.
54. Kodding, J., et al., *Crystal structure of a 92-residue C-terminal fragment of TonB from Escherichia coli reveals significant conformational changes compared to structures of smaller TonB fragments.* Journal of biological chemistry, 2005. **280**(4): p. 3022-8.
55. Sean Peacock, R., et al., *The solution structure of the C-terminal domain of TonB and interaction studies with TonB box peptides.* Journal of molecular biology, 2005. **345**(5): p. 1185-97.
56. Ahmer, B.M., et al., *Characterization of the exbBD operon of Escherichia coli and the role of ExbB and ExbD in TonB function and stability.* Journal of bacteriology, 1995. **177**(16): p. 4742-7.

57. Larsen, R.A. and K. Postle, *Conserved residues Ser(16) and His(20) and their relative positioning are essential for TonB activity, cross-linking of TonB with ExbB, and the ability of TonB to respond to proton motive force.* Journal of biological chemistry, 2001. **276**(11): p. 8111-7.
58. Carter, D.M., et al., *Interactions between TonB from Escherichia coli and the periplasmic protein FhuD.* Journal of biological chemistry, 2006. **281**(46): p. 35413-24.
59. Kampfenkel, K. and V. Braun, *Topology of the ExbB protein in the cytoplasmic membrane of Escherichia coli.* Journal of biological chemistry, 1993. **268**(8): p. 6050-7.
60. Nugent, T. and D.T. Jones, *Transmembrane protein topology prediction using support vector machines.* BioMed central bioinformatics, 2009. **10**: p. 159.
61. Jaskula, J.C., et al., *Role of the TonB amino terminus in energy transduction between membranes.* Journal of bacteriology, 1994. **176**(8): p. 2326-38.
62. Kampfenkel, K. and V. Braun, *Membrane topology of the Escherichia coli ExbD protein.* Journal of bacteriology, 1992. **174**(16): p. 5485-7.
63. Garcia-Herrero, A., et al., *The solution structure of the periplasmic domain of the TonB system ExbD protein reveals an unexpected structural homology with siderophore-binding proteins.* Molecular microbiology, 2007. **66**(4): p. 872-89.
64. Braun, V., et al., *Energy-coupled transport across the outer membrane of Escherichia coli: ExbB binds ExbD and TonB in vitro, and leucine 132 in the periplasmic region and aspartate 25 in the transmembrane region are important for ExbD activity.* Journal of bacteriology, 1996. **178**(10): p. 2836-45.
65. Fischer, E., K. Gunter, and V. Braun, *Involvement of ExbB and TonB in transport across the outer membrane of Escherichia coli: phenotypic complementation of exb mutants by overexpressed tonB and physical stabilization of TonB by ExbB.* Journal of bacteriology, 1989. **171**(9): p. 5127-34.
66. Higgs, P.I., P.S. Myers, and K. Postle, *Interactions in the TonB-dependent energy transduction complex: ExbB and ExbD form homomultimers.* Journal of bacteriology, 1998. **180**(22): p. 6031-8.
67. Braun, V. and C. Herrmann, *Point mutations in transmembrane helices 2 and 3 of ExbB and TolQ affect their activities in Escherichia coli K-12.* Journal of bacteriology, 2004. **186**(13): p. 4402-6.
68. Higgs, P.I., R.A. Larsen, and K. Postle, *Quantification of known components of the Escherichia coli TonB energy transduction system: TonB, ExbB, ExbD and FepA.* Molecular microbiology, 2002. **44**(1): p. 271-81.
69. Sauter, A., S.P. Howard, and V. Braun, *In vivo evidence for TonB dimerization.* Journal of bacteriology, 2003. **185**(19): p. 5747-54.
70. De Mot, R. and J. Vanderleyden, *The C-terminal sequence conservation between OmpA-related outer membrane proteins and MotB suggests a common function in both gram-positive and gram-negative bacteria, possibly in the interaction of these domains with peptidoglycan.* Molecular microbiology, 1994. **12**(2): p. 333-4.
71. Letain, T.E. and K. Postle, *TonB protein appears to transduce energy by shuttling between the cytoplasmic membrane and the outer membrane in Escherichia coli.* Molecular microbiology, 1997. **24**(2): p. 271-83.
72. Larsen, R.A., T.E. Letain, and K. Postle, *In vivo evidence of TonB shuttling between the cytoplasmic and outer membrane in Escherichia coli.* Molecular microbiology, 2003. **49**(1): p. 211-8.
73. Brockwell, D.J., et al., *Pulling geometry defines the mechanical resistance of a beta-sheet protein.* Nature structural biology, 2003. **10**(9): p. 731-7.

74. Gumbart, J., M.C. Wiener, and E. Tajkhorshid, *Mechanics of force propagation in TonB-dependent outer membrane transport.* Biophysical journal, 2007. **93**(2): p. 496-504.
75. Wagner, S., et al., *Rationalizing membrane protein overexpression.* Trends in biotechnology, 2006. **24**(8): p. 364-71.
76. Arechaga, I., et al., *Characterisation of new intracellular membranes in Escherichia coli accompanying large scale over-production of the b subunit of F(1)F(o) ATP synthase.* Federation of european biochemical societies, 2000. **482**(3): p. 215-9.
77. Garavito, R.M. and S. Ferguson-Miller, *Detergents as tools in membrane biochemistry.* The Journal of biological chemistry, 2001. **276**(35): p. 32403-6.
78. Erni, R., et al., *Atomic-resolution imaging with a sub-50-pm electron probe.* Physical review letters, 2009. **102**(9): p. 96-101.
79. Bozzola, J.J. and L.D. Russell, *Electron microscopy : principles and techniques for biologists*. 2nd ed, 1999, Sudbury, Massachusetts: Jones and Bartlett. **23**: p. 670.
80. Baker, M.L., et al., *Analyses of subnanometer resolution cryo-EM density maps.* Methods in enzymology, 2010. **483**: p. 1-29.
81. Baker, M.L., et al., *Cryo-EM of macromolecular assemblies at near-atomic resolution.* Nature protocols, 2010. **5**(10): p. 1697-708.
82. Erickson, H.P., *Size and shape of protein molecules at the nanometer level determined by sedimentation, gel filtration, and electron microscopy.* Biological procedures online, 2009. **11**: p. 32-51.
83. Kaito, M., et al., *Immune complex of hepatitis C virus particles detected by immunogold electron microscopy.* Journal of gastroenterology, 2006. **41**(8): p. 807-8.
84. Aebi, U. and T.D. Pollard, *A glow discharge unit to render electron microscope grids and other surfaces hydrophilic.* Journal of electron microscopy technique, 1987. **7**(1): p. 29-33.
85. Muhlfeld, C., *High-pressure freezing, chemical fixation and freeze-substitution for immuno-electron microscopy.* Methods in molecular biology, 2010. **611**: p. 87-101.
86. Greivenkamp, J.E., *Field guide to geometrical optics*. SPIE field guides, 2004, Bellingham, Washington: SPIE Press. **117**: p.67-71.
87. Fultz, B. and J.M. Howe, *Transmission electron microscopy and diffractometry of materials*. 3rd ed. Advanced texts in physics, 2008, Berlin; New York: Springer. **19**: p. 758.
88. Bochner, S. and K. Chandrasekharan, *Fourier transforms*. Annals of mathematics studies, 1949, Princeton: Princeton Univ. Press. **219**: p.287-91.
89. Reimer, L. and H. Kohl, *Transmission electron microscopy : physics of image formation*. 5th ed. Springer series in optical sciences, 2008, New York, NY: Springer. **16**: p. 587.
90. Grubb, D.T., *Review Radiation-Damage and Electron-Microscopy of Organic Polymers.* Journal of Materials Science, 1974. **9**(10): p. 1715-1736.
91. McMullan, G., et al., *Enhanced imaging in low dose electron microscopy using electron counting.* Ultramicroscopy, 2009. **109**(12): p. 1411-1416.
92. Chen, J.Z. and N. Grigorieff, *SIGNATURE: a single-particle selection system for molecular electron microscopy.* Journal of structural biology, 2007. **157**(1): p. 168-73.
93. Hohn, M., et al., *SPARX, a new environment for Cryo-EM image processing.* Journal of structural biology, 2007. **157**(1): p. 47-55.
94. Saxton, W.O. and J. Frank, *Motif Detection in Quantum Noise-Limited Electron-Micrographs by Cross-Correlation.* Ultramicroscopy, 1977. **2**(2-3): p. 219-227.
95. van Heel, M., et al., *Single-particle electron cryo-microscopy: towards atomic resolution.* Quarterly reviews of biophysics, 2000. **33**(4): p. 307-69.

96. Moeck, G.S. and J.W. Coulton, *TonB-dependent iron acquisition: mechanisms of siderophore-mediated active transport.* Molecular microbiology, 1998. **28**(4): p. 675-81.
97. Scheres, S.H., et al., *Maximum-likelihood multi-reference refinement for electron microscopy images.* Journal of molecular biology, 2005. **348**(1): p. 139-49.
98. van Heel, M. and M. Schatz, *Fourier shell correlation threshold criteria.* Journal of structural biology, 2005. **151**(3): p. 250-62.
99. Pettersen, E.F., et al., *UCSF Chimera--a visualization system for exploratory research and analysis.* Journal of computational chemistry, 2004. **25**(13): p. 1605-12.
100. Strop, P. and A.T. Brunger, *Refractive index-based determination of detergent concentration and its application to the study of membrane proteins.* Protein science, 2005. **14**(8): p. 2207-11.
101. D'Aoust, J.Y. and D.J. Kushner, *Structural changes during lysis of a psychorophilic marine bacterium.* Journal of bacteriology, 1971. **108**(2): p. 916-27.
102. Pramanik, A., et al., *ExbB protein in the cytoplasmic membrane of Escherichia coli forms a stable oligomer.* Biochemistry, 2010. **49**(40): p. 8721-8.
103. Tracz, E., et al., *Paired helical filaments in corticobasal degeneration: the fine fibrillary structure with NanoVan.* Brain research, 1997. **773**(1-2): p. 33-44.
104. Papahadjopoulos-Sternberg, B., *Freeze-fracture electron microscopy on domains in lipid mono- and bilayer on nano-resolution scale.* Methods in molecular biology, 2010. **606**: p. 333-49.